LASER-CARBONIZED GRAPHENE AND LIGNIN FILMS FOR SUSTAINABLE TRANSIENT RFID ELECTRONICS

JUVEIRIA KHAN

A THESIS SUBMITTED TO
THE FACULTY OF GRADUATE STUDIES
IN PARTIAL FULFILLMENT OF THE REQUIREMENTS
FOR THE DEGREE OF

MASTER OF APPLIED SCIENCE

GRADUATE PROGRAM IN MECHANICAL ENGINEERING

YORK UNIVERSITY
TORONTO, ONTARIO

SEPTEMBER 2025

Abstract

The growing problem of electronic waste calls for new materials that are sustainable and easy to recycle. This thesis focuses on developing conductive films for transient and flexible electronics using two different material systems.

In the first part, cellulose paper was used as a biodegradable base. Three types of coatings were prepared: (i) graphene oxide (GO), (ii) GO with ascorbic acid (AA) as a reducing agent, and (iii) GO with a mixture of ascorbic acid and sodium lignosulfonate (Na-Lgs) to provide extra carbon content. After coating, the samples were treated with a laser to create conductive patterns directly on the cellulose. This study shows that cellulose can serve as a compostable material for electronics while still offering useful electrical properties.

In the second part, polyethylene terephthalate (PET) films were coated with compressible flow exfoliated (CFE) graphene. PET provided strength and flexibility, while the graphene coating gave an initial conductivity that was further improved by laser carbonization. The PET/CFE system achieved very low sheet resistance, with the best value recorded at 16.17 Ω/sq, showing excellent electrical performance compared to many earlier studies.

To evaluate both systems, several techniques were used: SEM to study the surface and cross-section of the films, TGA to test thermal stability, Raman spectroscopy to analyze graphitic structure, FTIR to confirm chemical changes, and sheet resistance measurements to check electrical performance. Overall, the results show two promising directions: cellulose-based films for biodegradable and eco-friendly devices, and PET/CFE graphene films for high conductivity and robust performance. **In particular, the PET/CFE graphene system, with its low sheet resistance, shows strong potential for further development towards commercial RFID tags and other high-performance flexible electronic devices.**

Acknowledgements

I would like to express my sincere gratitude to my supervisor, **Professor Reza Rizvi**, for his continuous guidance, encouragement, and support throughout the course of my master's research at **York University**. His invaluable insights and constructive feedback have been instrumental in shaping this work and helping me grow as a researcher.

I would like to acknowledge **Aref** and **Agne**, whose prior work on this project laid an important foundation that greatly assisted my research. I am also grateful to my **group mates**, whose collaboration, discussions, and support made this journey both productive and enjoyable.

Finally, my heartfelt appreciation goes to my **family and friends** for their unwavering support, encouragement, and patience throughout this journey. Their constant belief in me has been my greatest source of motivation.

TABLE OF CONTENT

LIST OF TABLES

LIST OF FIGURES

Chapter 1: Introduction

1.1 Electronic Waste and Sustainability Challenges

The rapid advancement of technology has led to an increasing demand for electronic devices, many of which have short lifespans and contribute to growing environmental concerns regarding electronic waste (e-waste). Non-biodegradable materials, commonly used in electronics, pose a significant challenge to waste management and environmental sustainability [1]. Electronic waste not only occupies landfill space but also releases toxic materials into the environment during degradation, causing soil and water contamination. Globally, over 53.6 million metric tonnes of e-waste were generated in 2019 alone, with only 17.4% being formally collected and recycled [2]. The improper disposal of e-waste results in the leaching of toxic heavy metals such as lead, mercury, and cadmium into the environment, adversely affecting soil and water quality. As global e-waste continues to rise, there is an urgent need for the development of sustainable alternatives to conventional electronics that minimize environmental harm [3].

The most recent Global E-waste Monitor 2024, published by the United Nations University (UNU), reports that global e-waste production reached a record 62 million metric tons (Mt) in 2022, equivalent to about 7.8 kg per capita, a 38.7% expansion from the 44.7 Mt reported in 2016 [4]. Alarmingly, only 22.3% of this e-waste was officially collected and recycled using environmentally friendly processes. The yearly global e-waste generation is growing at a rate of about 2.6 Mt annually, with projections that it could reach 82 Mt by 2030, a 33% expansion relative to the levels seen in 2022 [4]. North America, and Canada and the United States in particular, remains a key contributor to this growing problem, producing an average of 20 kg of e-waste per

person in 2016. In Canada, this amounts to about 0.72 Mt of waste electronic equipment in that specific year [4].

1.2 Transient Electronics as a Solution

The low cost of raw materials for modern electronics makes recycling single-use or few-use devices economically impractical, while the cost of isolating the integrated elements in older electronics is higher. As a result, they are frequently dumped into the environment, where their toxic, xenobiotic (man-made) elements pollute the ecosystem or wind up in landfills [3].

Transient electronics, devices that can physically disappear or degrade in a controlled manner offer a promising solution to the e-waste crisis. These systems are typically fabricated from biodegradable, dissolvable, or compostable materials and are designed to perform for a predefined operational period before disintegration [2]. The relevance of transient electronics extends to applications in environmental sensors, biomedical implants, and military devices where device disappearance is beneficial. They align closely with the principles of the circular economy, minimizing end-of-life environmental burden by ensuring full material recyclability or biodegradability. The use of this technology has recently been extensively researched in a number of domains, including bioengineering, electronics, sensing, energy, and medicine [6–11]. Rasel et al. [12], for instance, created a rapid, one-step reduction method of graphene oxide (GO) on a metal substrate that allows the formed films to be functionally graded from conductive reduced-GO on one side to insulating GO on the other. Because GO is naturally water-dispersible, the electronically conductive sheets may dissociate in water more easily, forming a uniform, recyclable suspension. Another work by Kwon et al. [11] introduces a recyclable conductive composite material based on enzyme/protectant nanoclusters, polycaprolactone (PCL), and silver

fillers that can be broken down in warm water for application in printed transient electronics. Almost 94% of the decomposed materials can be reused to manufacture electronics that possess the same functionality.

1.3 Objectives

The majority of laser carbonization precursors utilized in the literature are non-renewable and relatively costly, and the qualities of the final material are constrained by polymeric materials. Bio-based products, such as lignin and its derivatives, are being researched as available, affordable, and safe alternatives to address this issue. Using a CO2 laser in a specialized environment, Tour's team has demonstrated that it is possible to get high conductivity by turning wood into so-called laser scribed graphene (LSG) at a cheap cost [49]. In another study conducted by Lei et al, MXene-based spray coating of carbonized lignin/PVA/urea composite was used to create highly conductive LSG for sensing applications.[54]. Although promising materials and methods for producing transient electronics have been demonstrated, the current methods have limited practical applicability due to either poor mechanical and electrical properties or a labor-intensive and complicated production procedure.

To bridge this gap, this research centers on two studies: cellulose coated with graphene oxide and lignin-based blends, and PET films with compressible flow exfoliated (CFE) graphene coatings. They were chosen to achieve environmental sustainability and robust electrical performance. This work is based on an objective triangle (Figure 1), which sets out three essential requirements. The first is biodegradability or recyclability, ensuring that the developed devices minimize electronic waste. The second is manufacturing freedom, where the fabrication process must be fast, straightforward, and adaptable to produce complex circuit patterns. The third is high conductivity,

which is necessary for efficient operation in applications such as RFID antennas and other flexible electronic components.

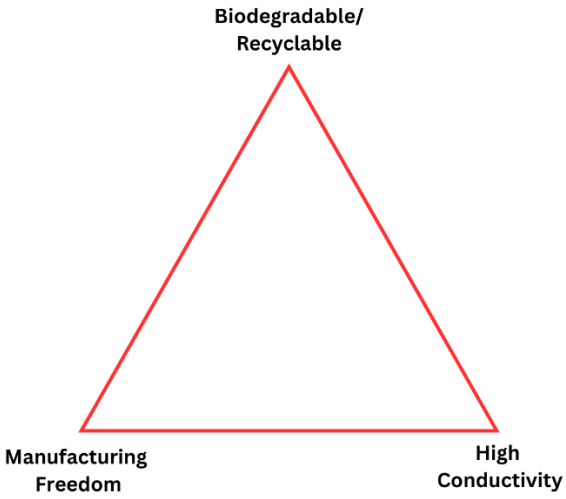

Figure 1: Schematics of objectives triangle. The top vertex refers to the biodegradability of the film and the second one shows the manufacturing method ability to create complex shapes and last one is to achieve high conductivity.

1.4 Scope of the Study

This research focuses on two main studies to create conductive and environmentally friendly films. The first study centres on four key materials: graphene oxide for its high conductivity potential, ascorbic acid as a reducing agent, lignosulfonate as a biodegradable carbon-rich component, and cellulose as a flexible and compostable substrate. The second study uses PET sheet coated with compressible flow exfoliated (CFE) graphene. In this case, the PET provides strong mechanical support, and the CFE graphene layer acts as an initial film that is further improved through laser carbonization. By studying both cellulose and PET-based coatings, the work compares a fully

biodegradable option with a highly conductive but less degradable alternative. Together, these two approaches help in understanding how to balance sustainability with electrical performance for applications such as transient RFID and single-use electronic devices. Laser-carbonization has been chosen as a rapid, economical, and flexible design production technology due to its multiple advantages. First, laser carbonization is highly controlled by changing parameters such as laser speed, power, beam focus height, and wavelength. An immediate high-energy laser may carbonize various carbon-based precursor materials. In this thesis, a laser with varied characteristics is used to carbonize different compositions in order to develop and optimize highly conductive transient electrical circuits. Thermogravimetric Analysis (TGA), Fourier Transform Infrared (FTIR) Spectroscopy, Raman Spectroscopy, and Scanning Electron Microscopy (SEM) were used to describe the characteristics. These techniques showed the samples' morphology and degree of carbonization. The samples were then subjected to four-point probe tests in order to determine the sheet resistance. As a proof-of-concept, a coil-shaped RFID tag is created, optimized, produced, and tested after the composition and laser settings are adjusted. Finally, to illustrate the film's transience and disintegration qualities, it was submerged in water, and the performance of the film's degradation was tracked over time.

1.5 Thesis Organization

This thesis is structured into seven chapters. Following this introduction, **Chapter 2** reviews existing literature on transient electronics, biodegradable materials, and RFID sustainability. **Chapter 3** outlines the materials and methods used in preparing and processing graphene-lignin films. **Chapter 4** presents the characterization and performance analysis of laser-carbonized films. **Chapter 5** explores an alternative graphene synthesis method using compressible-flow

exfoliation. **Chapter 6** focuses on the design, fabrication, and testing of RFID antenna prototypes. **Chapter 7** concludes the study with key findings, limitations, and recommendations for future research.

Chapter 2: Literature Review

2.1. Sustainable and Transient Electronics

As the demand for sustainable solutions in electronics grows, transient electronics have emerged as an innovative response to the challenges of electronic waste. These systems are fabricated using biodegradable or dissolvable materials that decompose under specific environmental conditions, significantly reducing their ecological footprint. The integration of such electronics into real-world applications, ranging from biomedical implants to environmental sensors which has been gaining traction due to their compatibility with circular economy principles [4]. Research in this domain emphasizes the need for multifunctional materials that combine environmental friendliness with acceptable electronic performance.

The use of biodegradable polymers and natural compounds is central to the development of transient electronics. Materials such as polylactic acid (PLA), cellulose derivatives, and silk fibroin have shown promise due to their biodegradability, mechanical flexibility, and compatibility with printing or coating techniques. These materials can serve as substrates, dielectric layers, or encapsulants in electronic devices, enabling full-device degradation post-use. Their integration has been widely studied in the context of sensors, batteries, and even transistors [5]. The biodegradation process can be tailored by adjusting polymer composition, thickness, or exposure to environmental triggers such as moisture or enzymes, making them highly adaptable for eco-electronics.

For practical applications, especially in wearable and flexible electronics, mechanical durability is just as critical as biodegradability. Materials used in transient devices must withstand bending,

stretching, and twisting without significant degradation in performance. Studies have shown that laser-carbonized graphene-lignin composites exhibit favourable flexibility and can retain conductivity under cyclic deformation, making them suitable for foldable electronics and flexible RFID antennas [6]. The mechanical properties are influenced by film thickness, carbonization quality, and substrate compatibility, emphasizing the need for integrated mechanical-electrical optimization.

Radio-frequency identification (RFID) is a universal technology used in logistics, inventory management, and contactless systems. Conventional RFID tags are typically fabricated using metals like copper and aluminium on plastic substrates, which pose recycling and environmental challenges. The development of biodegradable and metal-free RFID tags addresses these limitations by utilizing sustainable materials and fabrication methods. Biocompatible substrates combined with carbon-based conductors can achieve comparable functionality while enhancing environmental safety [7]. These advancements open pathways for integrating transient RFID systems into sustainable supply chains and smart packaging solutions.

2.2. Graphene and Its Applications in Electronics

2.2.1 Graphene and its Conductive Properties

Graphene has attracted considerable attention in the field of electronics due to its exceptional electrical conductivity, high carrier mobility, and excellent thermal conductivity [11]. These properties make it suitable for use in transistors, sensors, and flexible electronics. In particular, graphene oxide (GO), a chemically modified derivative of graphene, can be reduced via thermal, chemical, or laser-induced methods to form reduced graphene oxide (rGO) with improved

conductivity. Laser reduction is especially promising because it enables spatially selective patterning and simultaneous carbonization, making it a scalable and environmentally benign process [12].

The hypothesis of two-dimensional crystals was tested in 2004 when Novoselov et al. [13] successfully separated graphene from the monolithic form using a mechanical peeling technique. Graphene's structure is a planar hexagonal lattice. Three (2s, 2px, and 2py) of the four valence electrons that make up each carbon atom form planar sp2 hybrid orbitals. The final orbital electron is free to go through the plane after forming a strong π bond. It is a two-dimensional carbonaceous material with a hexagonal honeycomb crystal structure. Graphene is currently the thinnest and most resilient nanomaterial available today, with a sheet thickness of 0.34 nm [14]. Graphene has a short C-C bond length (0.142 nm) and a stable structure [15]. When electrons move in internal orbits, there is no scattering due to interference from outside atoms or lattice defects [16], [17]. Because of its unique planar lattice structure, graphene has several amazing qualities, including great mechanical stiffness (Young's modulus of 1 TPa) and high electrical conductivity (106 S/m) [18]. Although there are several methods for producing graphene these days, the most popular ones include redox processes, chemical vapour deposition, mechanical and liquid phase exfoliation, and epitaxial growth [19].

2.2.2 Graphene Oxide and its Reduction Mechanism

Graphene oxide is the oxidised version of graphene, a two-dimensional carbon molecule with a single atomic layer and polydisperse sheet sizes. Simple processing, large manufacturing, and low production costs are the advantages of graphene oxide (GO) over graphene [20]. Graphene oxide's structure is more complicated due to the presence of oxygen-containing functional groups, and its

structure affects these properties [21]. In addition to having an oxygen-based functional group like hydroxyl (-OH), alkoxy (C-O-C), carbonyl (C=O), carboxylic acid (COOH), and others, graphene oxide (GO) has a hexagonal carbon structure with graphene. Depending on the requirements of certain application domains, these oxygen-containing groups or reduced doping components can be used as catalytic active centres for the creation of covalent or non-covalent modifications. Additionally, the presence of oxygen-containing groups widens the graphene oxide interlayer gap. The structural properties of graphene oxide are described by the L-K model, which was developed by Lerf [22]. It is demonstrated that whereas the hydroxyl and epoxy groups are randomly distributed across the graphene oxide's basal plane, the carboxyl and carbonyl groups are added to the edge of the single layer.

Sheet peeling and oxidant intercalation are typically the two processes utilised to create graphene oxide. This process initially oxidises graphite with a variety of chemicals (such as HNO3 and KClO3), creating oxygen functional groups on the graphene-like sheets. After that, the oxidised sheets undergo exfoliation, producing 2D graphene oxide sheets. Their outstanding electrical, mechanical, and thermal capabilities are a result of graphene and graphene oxide's remarkable structural and morphological features [23–25].

Reduced graphene oxide (rGO), an electrically conductive graphitic carbon, can be created from graphene oxide (GO) by removing the functional groups using a variety of reduction techniques, including (electro)chemical , thermal , hydrothermal, and photothermal(Figure 2).

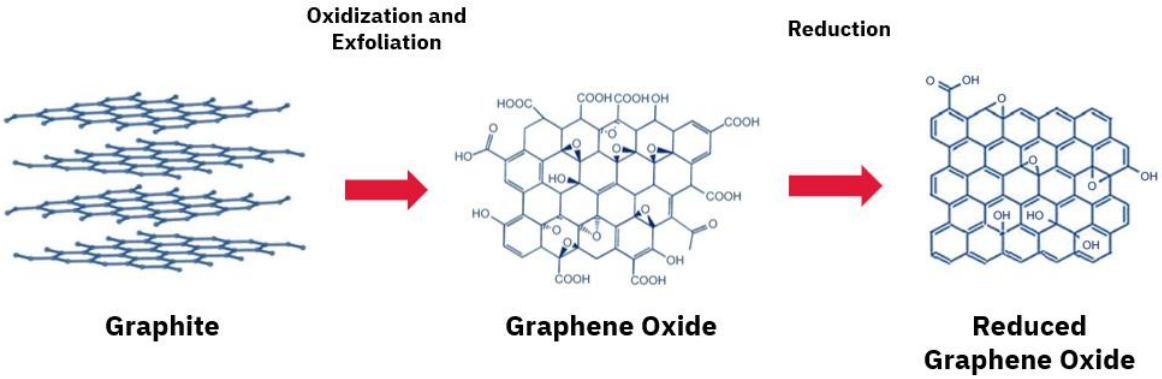

Figure 2: From Graphite to reduced-GO

Numerous studies on graphene oxide reduction techniques have been carried out, including advanced methods like electrochemical and laser-assisted techniques as well as chemical and thermal techniques. The Hydroiodic (HI) Acid-assisted approach for graphene oxide reduction was published by Pei et al. [29] and demonstrated a C/O ratio greater than 12. The significant impact of HI Acid on GO reduction is confirmed by the low sheet resistance (1.6 k-ohm/sq) of the produced rGO films, which is especially low when compared to other earlier chemical techniques. Moreover, it has been documented that GO films on any substrate may be effectively reduced by a laser beam [20]. Guan et al. [30] employed a laser beam to reduce graphene oxide (GO) in order to achieve a high conductivity (727 S m-1) on the reduced portions of their study on laser-induced graphene oxide reduction. Huang et al. [31] have demonstrated that when GO comes into touch with a metal powder or sheet (such as aluminium), it may be significantly reduced and self-assemble. One example is the fabrication of a broad graphene layer at 900 °C with copper foil present, which was then annealed in an environment containing H2. Metal-assisted reduced films' electrical characteristics (3.6x104 S/m) indicate encouraging possibilities for flexible electronics applications.

2.3. Sodium Lignosulfonate

Lignin, a major byproduct of the paper and bioethanol industries, is an abundant, renewable, and aromatic biopolymer. It is characterized by a complex phenolic structure, making it rich in carbon and suitable for conversion into conductive carbon-based materials. Recent studies highlight lignin's potential as a precursor for the fabrication of carbon-rich conductive films when subjected to processes like pyrolysis or laser scribing [30]. By leveraging lignin's natural abundance and biocompatibility, researchers aim to replace synthetic, non-degradable materials in electronic applications, aligning well with the goals of sustainable development. It is possible for lignin to be sulfonated to lignosulfonate, which is water soluble and anionically charged due to the presence of the sulfonated group. Due to their special qualities, lignosulfonates are used in many different applications, such as plasticizers in concrete admixtures, animal feed, pesticides, surfactants, oil drilling additives, and colloidal suspension stabilisers [34].

2.4. Cellulose as a Substrate for Electronics

Cellulose offers a biodegradable and flexible platform for transient electronic devices. Its film-forming capabilities and chemical compatibility make it an excellent substrate for coating and patterning processes. Moreover, its ability to degrade in natural environments like soil or water enhances the sustainability profile of any electronic device fabricated on it[38]. The use of cellulose acetate in conjunction with laser-based fabrication techniques enables the development of low-waste, eco-friendly electronics. Cellulose materials for electronics are prepared by using various grades of cellulose, including nanofibrils, microcrystalline cellulose, and all-cellulose composites. These are characterized by different mechanical, chemical, and optical behaviour when it comes to device integration. Preparation involves commonly applying techniques such as

hot-pressing, casting, or blending inorganic dyes with nanocellulose in order to form a substrate. Such a substrate is flat with a non-porous surface and is extremely ductile. Preparation techniques in some cases involve heat and pressure in an attempt to enhance stability as well as quality in surface for stable device assembly. When in preparation, surface characteristics such as porosity as well as uniformity are strictly regulated. Such characteristics are significant in printability as well as in depositing conductive tracks, metal contacts, as well as electronic components with means such as UV photolithography and inkjet printing.

2.5. Laser Carbonization for Electronics

Carbonization has generally been achieved by pyrolysis or hydrothermal methods [35]. The quality of the resultant products is determined by the precursors, reaction conditions (e.g. temperature, pressure, duration), and synthesis environment. Laser-carbonization technology has the potential to extend the use of carbonised materials in film electronics [36]. Laser carbonization involves the localized conversion of organic or polymeric materials into carbonaceous structures through high-energy laser irradiation. This technique allows precise patterning of conductive features on flexible substrates without the need for masks or etching processes. The extent of carbonization can be modulated by controlling laser parameters such as wavelength, power, and scanning speed. Laser carbonization is especially useful for integrating carbon-based conductors into transient electronic devices due to its rapid, solvent-free, and scalable nature [38].

LIG is formed by photothermally converting carbonaceous materials like polyimide (PI), polyetherimide (PEI), phenolic resin, wood, paper, cork, polysulfone (PSU), lignin, and even biopolymers and fabrics using a laser source. This method is increasingly used in 3D printing [18]. Localised heating destroys chemical bonds and creates very porous graphene. The laser preferably

transforms the top layer of the precursor material to a graphitised structure, eliminating the need for additional catalysts [17].

LIG's primary qualities that have made it a promising material for a variety of applications are: Porous Structure, High Conductivity and Tuneable Properties. Ion transport is facilitated by the three-dimensional porous graphene network of LIG, which can improve the electrochemical performance of electrodes with a large surface area [20]. LIG's strong electrical conductivity, which makes it appropriate for electronic and sensing applications, is a result of its sp2-hybridized carbon network [14]. By adjusting laser processing parameters like as scan speed, power, and wavelength, the material characteristics of LIG may be tailored for particular applications [17]. LIG is a material that is becoming more and more popular in a variety of disciplines because of its distinct structural and electrochemical characteristics, which make it a possible substitute for traditional graphene-based electrodes. El-Kady et al. [48] demonstrated the scalable production of graphene micro supercapacitors over wide regions using a regular LightScribe DVD burner and direct laser writing on graphite oxide sheets with a conductivity of 2.35×10^{3} S m−1. At 200 W cm-3, these tiny supercapacitors have one of the greatest power densities of any supercapacitor. Another work using laser induction to produce 3D porous graphene sheets from polymers was carried out in the group of Professor James Tour [49]. A Polyimide (PI) film was graphitized with a commercial CO2 laser to achieve a sheet resistance of less than 15 /sq. Following the earlier work, Liu et al. [50] demonstrated a high-efficiency technique for creating Fe3O4 nanoparticle-anchored laser-induced graphene (LIG/Fe3O4) with hierarchical porous structures on a flexible PI substrate. This method involves laser-deposition of aggregated Fe3O4 nanoparticles (24.08 nm) with mesopores onto macroporous LIG scaffolds in a single step, yielding a conductivity of 17.16 S cm-1. Furthermore, Zhang et al. [45] devised and used a straightforward lignin-based laser

lithography technique to construct on-chip micro-supercapacitors (MSCs) with three-dimensional graphene electrodes. 3D laser-scribed graphene (LSG) electrodes are created directly from lignin sheets using a simple one-step CO2 laser irradiation process. The resulting LSG electrodes have a high specific surface area of 338.3 m2 g-1, a hierarchical porous structure, and an electrical conductivity of up to 66.2 S cm-1. Additionally, Kulyk et al. [51] created strain and bending sensors by using a CO2 laser to irradiate ordinary filter paper. The created material includes web-like, porous structures that transmit electricity, and its sheet resistance is as low as 32 Ω/sq. The dependable real-time response of these devices to the specified physical conditions validates graphene's potential for inexpensive and environmental sensing devices. Another recent research by Yuan et al. [52] proposed a scalable, easy, and efficient way to use laser direct writing on a precursor-doped polyimide (PI) surface to create in situ heteroatom-doped porous graphene. Using a drop-casting and low-temperature drying technique, PI powder and precursors were mixed with a sodium carboxymethyl cellulose (CMC) binder for the first time, indicating a conductivity of 39.5 S cm-1. Furthermore, kraft lignin was used as a precursor in this group's previous effort to produce laser-induced graphene sheets that might be used in flexible supercapacitors [53].

Laser-scribed carbon materials, particularly those derived from graphene oxide and lignin blends, have shown competitive electrical properties for low-power electronics. Parameters such as sheet resistance, conductivity, and signal attenuation are critically influenced by the degree of graphitization, which in turn depends on laser intensity and exposure time. These carbon-based films demonstrate sufficient conductivity for use in RFID antennas, sensors, and energy storage devices. Importantly, unlike traditional metal-based conductors, laser-scribed films are more environmentally benign and support additive manufacturing processes with minimal waste.

In laser-induced graphene research, different types of lasers have been used depending on the material and the level of precision required. For example, CO_2 lasers were the first to be used on polyimide by James Tour group and are still considered the benchmark, while infrared laser is popular for fast, high-power writing. More recently, green and blue lasers have been explored because they interact better with natural and biodegradable substrates like cellulose and lignin. There are also UV lasers that can achieve very fine features but are expensive and slow.

Table 1: Laser technologies used in LIG: applications, pros & cons

Laser Type	Wavelength	Pros	Cons
CO_2 Laser	10.6 µm (IR)	• widely available • Strong absorption in PI	•Burns too deep (thermal damage) • Limited resolution (tens of µm) • Poor for transparent/organic films
Green Laser	532 nm	• Better absorption on organics than IR • Finer resolution than CO_2	•Machines cost more •Lower power than CO_2
Blue Laser	445–488 nm	• Very good absorption in carbon materials • Fine lines (<10 µm) • Small, low-cost systems available	•Lower power (few watts) •Only affects surface layer (shallow)
UV Laser (Excimer)	355–193 nm	• Very fine features (micro-scale) • Almost no heating → less damage	•Very expensive •Slow processing, complex maintenance

Chapter 3: Material Preparation and Experimental Methods

3.1 Materials Selection and Preparation

The selection of materials for transient and sustainable electronics hinges on their biodegradability, electronic functionality, and compatibility with green fabrication techniques. In this study, **graphene oxide (GO)**, **lignosulfonate (Na-LgS)**, and **cellulose** were chosen due to their environmentally benign profiles and ability to synergize in forming conductive, degradable films.

In this work, the films on Cellulose were created using highly concentrated graphene oxide and sodium lignosulfonate materials. We bought GO dispersion (2.5 weight percent) from Sigma-Aldrich. According to the company's study, the material's attributes include >95% monolayer content determined in 0.05 weight percent aliquot and a D90 particle size of 29–33 μm. The source of the Na-LigS utilised in this investigation is also from Sigma-Aldrich. **Fisher brand Weighing Paper** (Figure 3) is used as a substrate, which had a thickness of 85μm and is specifically designed for laboratory use to accurately measure and transfer dry chemicals, powders, or granules without contamination. It is a low-nitrogen, high-purity cellulose paper without any coating.

Figure 3: Cellulose-based weighing paper (Fisher brand, 4×4 inch) used as the substrate material for coated precursor films for laser carbonization and subsequent formation of laser-induced graphene (LIG).

3.1.1 Graphene Oxide and Lignosulfonate Solution Synthesis

For this study, three different types of precursor coatings were set up on cellulose paper substrates in order to test their potential for laser-induced carbonization. The first sample was a pure coating of graphene oxide (GO) in its standard form as a control material for comparison for the basic characteristics of laser-converted graphene. As a secondary sample, it was prepared by adding ascorbic acid (AA) into a GO solution based on its reducing ability allowing for partial conversion of GO into reduced graphene oxide in advance of laser treatment to improve conductivity. As a third sample, it combined GO with ascorbic acid (AA) as above plus an addition of lignin-derivative sodium lignosulfonate (Na-Lgs), a compound noted for its polyaromatic nature as a suitable component for combination with GO which would improve graphitization and stability upon exposure to laser treatments.

GO (2.5 wt%) was concentrated to 3.5 wt% by evaporating water through heating the mixture in a beaker and on a hotplate stirrer at 40ºC (Figure 4-a). For the second sample formulation, 3 wt% ascorbic acid (AA) was added into the graphene oxide (GO) combination. The combination was continuously stirred at 60 °C for 3 hours in order to ensure it was thoroughly mixed and for GO and AA to engage ideally (Figure 4-b). This step served to partially convert GO into reduced graphene oxide (rGO) prior to the laser processing. It would enhance the reduction effectiveness as well as raise the conductivity of the end laser-carbonized film.

For the third formulation, first powder-form sodium lignosulfonate (Na-Lgs) was slowly added to deionized water in order to form a 50 wt% solution of Na-Lgs. That Na-Lgs solution was then combined with the GO–AA dispersion in a ration 30wt%GO and 70wt% Na-Lgs Solution, and it was then stirred at room temperature for 2 hours to ensure everything was fully combined and

evenly dispersed (Figure 4-c). Including Na-Lgs, which itself not only had a complicated structure but was also capable of mixing with water, should have assisted in keeping sheets of GO separated throughout carbonization in the subsequent laser treatment.

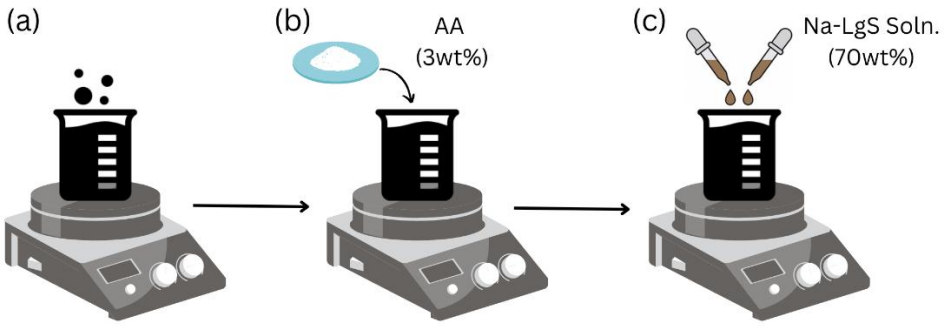

Figure 4: Schematic illustration of the preparation steps: (a) graphene oxide (GO, 2.5 wt%) dispersion heated on a hotplate stirrer at 40 °C to concentrate it to 3.5 wt%, (b) addition of 3 wt% ascorbic acid (AA) into the GO dispersion and stirring at 60 °C for 3 h to partially reduce GO into rGO, and (c) incorporation of sodium lignosulfonate (Na-Lgs, 70 wt% solution) into the GO–AA mixture, followed by stirring at room temperature for 2 h to ensure complete dispersion.

3.1.2 Coating Process on Cellulose based substrate

A carbon-based precursor ink was coated using the produced gelatinous solutions. On the cellulose substrate, a sufficient quantity of ink was doctor bladed with a wet thickness of 500 µm. After that, the assembly was heated to 60 °C for two hours to create a dry film that was about 20±1 µm thick.

3.2 Laser Carbonization

Laser carbonization was employed to selectively convert the coating into conductive carbon patterns. This step is crucial for patterning functional components such as RFID antennas without the use of harmful chemicals or masks. During this process, the dried substrate is subjected to a

blue laser (λ = 450 nm) to carbonize the lines drawn on the material. The Snapmaker 2.0 A350T (Figure 5) laser equipment is used for this purpose due to its versatility and precision. According to the Snapmaker technical documentation the spot size range is 0.2 mm x 0.3 mm. This equipment allows for fine-tuned control over the carbonization process, enabling adjustment of the laser's intensity and duration to achieve optimal conductivity in the carbonized lines. The laser-carbonized areas were visually darkened, and their conductivity was confirmed using a four-point probe technique, as detailed in Chapter 4.

The laser power of the Snapmaker blue laser module is modulated using Pulse Width Modulation (PWM). This means that the power setting expressed as a percentage (e.g., 50% power) corresponds to the duty cycle of the PWM signal applied to the laser diode driver. A 50% power setting means the laser is on for 50% of the PWM cycle and off for 50%, but this switching happens at a very high frequency, so the output appears continuous.

Figure 5: The Snapmaker 2.0, A350T 3in1 laser machine.

3.2.1 Film Preparation and Laser Parameters

The main variables considered for optimization in this study include both material formulations and laser processing parameters (Table 2). The details of the fabrication process of laser-carbonized films are demonstrated in Figure(6).The initial phase involves the application of a film coating (Step 1), during which the precursor formulations: GO, GO + AA, and GO + Na-Lgs + AA are evenly applied to the cellulose paper substrate utilizing the doctor blade method to achieve a controlled film thickness. The thickness of the coated material can be controlled by doctor blade as two micrometres attached to the blade which recognises the height of the blade from the substrate surface. Subsequently, the coated films are subjected to a drying procedure (Step 2) at 60 °C for a duration of two hours on a hot plate, a constant condition upheld for all samples to eliminate residual moisture and enhance the adhesion of the precursors. Once dried then films are subsequently subjected to laser carbonization (Step 3), where a concentrated laser beam is passed through the film face at changing power and speed levels. This step is crucial for inducing localized carbonization, resulting in the formation of conductive laser-induced graphene (LIG) patterns. Electrical properties of films that have undergone laser carbonization are subsequently characterized using the four-point probe method (Step 4). This technique gives reliable sheet resistance measurements through the exclusion of the effect of contact resistance and hence providing a means of reliable determination of the effect of precursor species and laser treatment conditions on the level of conductivity.

Table 2:Experimental parameters and conditions for the fabrication of laser-induced graphene (LIG) on coated cellulose substrates.

Category	Parameter	Notes
Precursor	GO, GO + AA, GO + Na-Lgs + AA	3 Formulations
Substrate	Cellulose paper	Fixed
Drying	60 °C for 2 hours (fixed)	Fixed
Laser Power	Low (10%), Medium (30%), High (80%)	3 Levels
Laser Speed	Slow (500 mm/s), Medium (1000mm/s), Fast (1500 mm/s)	3 Levels
Focus Distance	+1 mm	Fixed

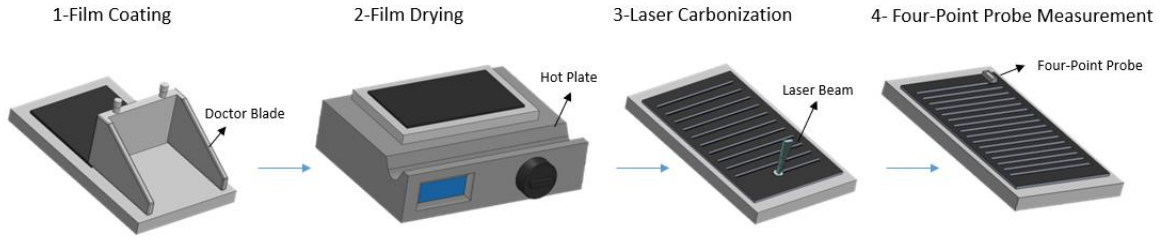

Figure 6: Schematic drawings of coating on the substrate, film drying, laser carbonization and four-point probe measurement for sheet resistance.

Chapter 4: Material Characterization

4.1 Surface Morphology Analysis Using Scanning Electron Microscopy (SEM)

Scanning Electron Microscopy (SEM) was employed to investigate the surface morphology and porosity of the laser-treated graphene oxide composite films. SEM images revealed that the laser scribing process induced a porous and wrinkled texture across the irradiated regions, indicative of localized thermal decomposition and carbon formation. These morphological features enhance surface area and electrical conductivity, which are advantageous for RFID antenna applications.

4.1.1 GO Coated on Cellulose Paper

The SEM images of GO-coated cellulose (Figure 7) clearly show the natural paper substrate's fibrous texture. The cellulose fibres are still very visible, which means that the GO coating is patchy and discontinuous. GO is seen on the surface as thin plate-like flakes draped over the fibre walls. The flakes are not continuous but rather overlap irregularly, with some areas bare and others covered densely. Wrinkles and folds can also be observed on the sheets, a characteristic of graphene oxide given its flexible nature. The coating overall thus appears heterogeneous with alternating smooth GO-rich patches and rough cellulose-rich patches.

The cross-sectional images give additional information (Figure 8). They show that the GO mainly adheres to the exterior surfaces of the fibres, making a very thin coating. Penetration into the porous inside of the paper is slight, and most of the inter-fibre voids are not filled. The GO is found concentrated at intersections of fibres, where mechanical contact allows it to adhere. So, prior to carbonization, the GO layer is more of a surface deposition than a continuous film. Following laser

carbonization, the morphology is radically altered. The smooth flake-like GO is converted into a rough, porous carbon layer. The localized laser heat causes instant decomposition of oxygen groups, generating intense gas release. This forms microcracks, voids, and pores, which appear in the SEM images as dark, roughened areas. At the surface, the carbonized tracks form a continuous band, bridging neighbouring fibres that were previously only loosely coated. The cross-section reveals a thin darkened layer over the fibre perimeters, clearly outlining the carbonized area. The penetration depth is, however, limited, and most of the carbonization is focused close to the fibre walls. The outcome is a conductive but brittle porous carbon structure, heavily determined by the discontinuous nature of the starting GO coating.

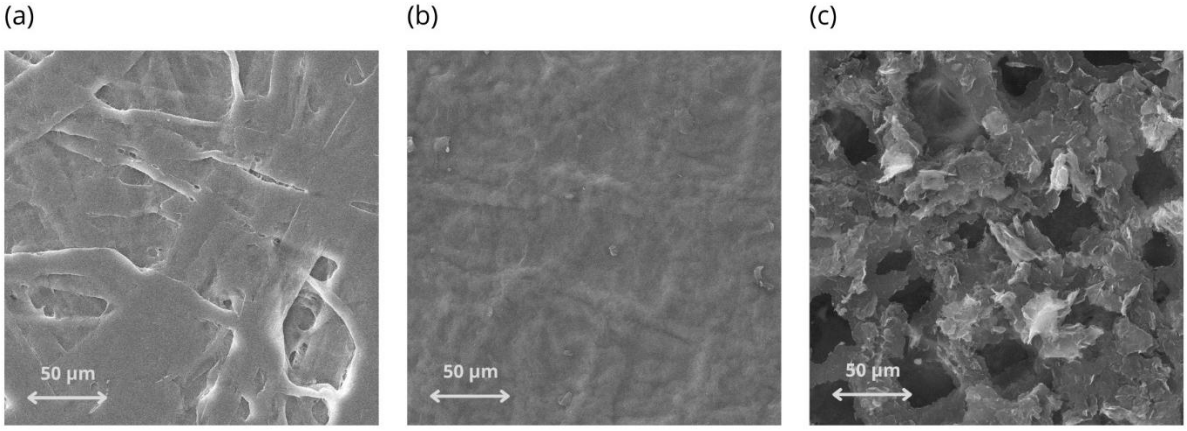

Figure 7: SEM images of cellulose substrate and GO-coated films: (a) bare cellulose surface showing fibrous morphology, (b) uniform coverage of graphene oxide (GO) on cellulose, and (c) porous laser-carbonized GO structure after laser treatment.

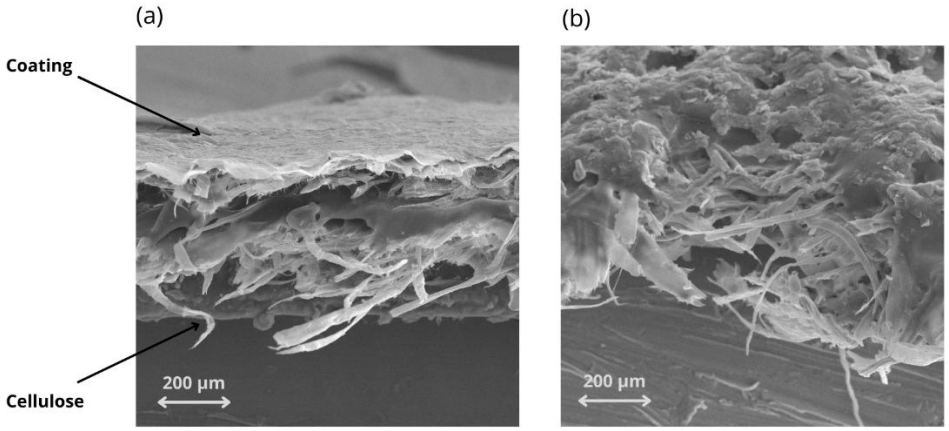

Figure 8: Cross-sectional SEM images of cellulose-based substrate: (a) GO coating layer deposited on cellulose surface, showing distinct coating and substrate interface, and (b) porous morphology after laser carbonization of the GO layer.

4.1.2 (GO + Ascorbic Acid) Coated on Cellulose Paper

The SEM images of the GO + Ascorbic Acid coated cellulose (Figure 9) show a significantly more uniform surface morphology than GO alone. The coating on the surface looks smoother and more continuous, with less exposed cellulose spots. This is due to the partial reduction of GO by ascorbic acid, which promotes sheet-to-sheet stacking and adhesion on the fibres. The flakes overlap more closely, yielding a denser covering. At a higher magnification, tiny shrinkage cracks are visible across the film, which is a consequence of water evaporation and densification upon drying. These cracks, however, are fine and do not undermine the general uniformity of the coating.

The cross-sectional view (Figure 10) shows that the incorporation of GO and AA yields a thicker layer coating the fibres. Compared with the GO-only sample, this coating also exhibits better wetting on cellulose and continues along the fibre surfaces, leading to a denser structure. Furthermore, a few thin layers are observed to bridge small gaps between adjacent fibres,

indicating better film development. The thickness of the coating appears to be larger than that of the GO-only sample, suggesting higher loading and adhesion. On laser carbonization, the surface turns uniformly dark and textured but with finer and more compact porosity than the GO sample. The fewer oxygen groups (introduced by ascorbic acid in reduction) result in less volatile gas being released during laser heating, creating smaller and more controlled pores. This yields a smoother carbonized track with fewer defects and cracks. The cross-section shows that the carbon layer is also better adhered to the cellulose fibres, with more uniform thickness and fewer discontinuities at fibre junctions. This closer adhesion between the carbonized coating and cellulose support imparts the film with better mechanical integrity. Overall, the GO+AA system demonstrates a marked improvement over GO alone in terms of uniformity, carbonization stability, and interfacial bonding.

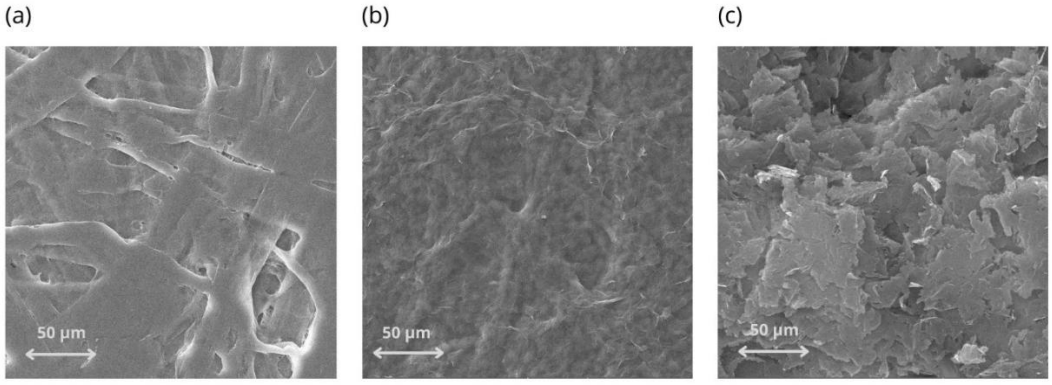

Figure 9: SEM images of cellulose-based substrates: (a) bare cellulose surface, (b) cellulose coated with GO+AA showing a smoother and more compact film, and (c) porous and wrinkled morphology of GO+AA layer after laser carbonization.

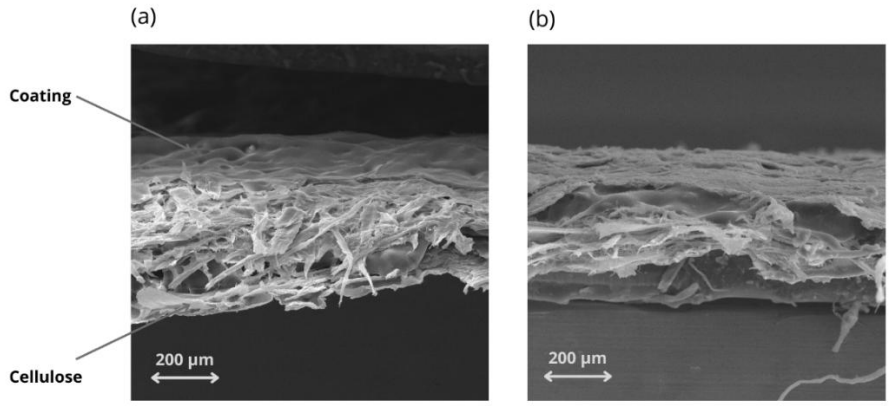

Figure 10: Cross-sectional SEM micrographs of cellulose substrates with GO+AA coating: (a) uniform GO+AA coating layer adhered to the fibrous cellulose network, highlighting the layered morphology at the interface, and (b) post-laser carbonization structure, showing increased porosity and partial disruption of the coating due to laser-induced graphitization.

4.1.3 (GO + Ascorbic Acid + Sodium Lignosulfonate) Coated on Cellulose Paper

The addition of sodium lignosulfonate radically alters the film morphology both prior to and following laser treatment. The as-coated film surface SEM (Figure 11) reveals that the cellulose fibres are well masked by a continuous coating, with the additive functioning both as a binder and dispersant. This results in a smoother, more uniform film relative to GO or GO+AA. Rounded nodular features are apparent, which most probably represent lignosulfonate-rich domains that serve to fill voids and enhance coverage over the fibre network.

The cross-sectional images (Figure 12) demonstrate that this sample has the most considerable and coherent coating layer of the three cellulose-based systems. The film successfully bridges the gaps between fibres, forming a continuous scaffold with a strong adhesion to the substrate fibres. Unlike the limited coating observed for the GO-only system or the medium coverage observed with

GO+AA, the GO+AA+Na-LgS film is described as a noteworthy layer that partially penetrates the porous structure, reducing the gap between coating and substrate.

Following laser carbonization, the morphology is subjected to intense foaming. Decomposition of the lignosulfonate involves intense gas evolution, creating a very porous, sponge-like carbon morphology. The surface SEM reveals a heterogeneous pore distribution, ranging from small micro-pores to larger voids. Although the carbon layer is still well attached to the substrate, these irregular voids compromise the compactness of the network. In cross-section, the carbonized band is thicker and darker than the other samples, attesting to deeper carbonization. Nevertheless, localized pore collapse and bigger voids can also be seen, revealing that although the carbon skeleton is solid, its continuity is partially compromised. In short, the GO+AA+Na-LgS system produces a film that is both mechanically strong and has a strong adhesion to cellulose, but its microstructural properties show a trade-off between thickness and porosity. The dense carbon layer provides a substrate and stability, but the non-uniform foaming reduces the density of the conduction paths compared to the more delicate and homogeneous structure of the GO+AA sample.

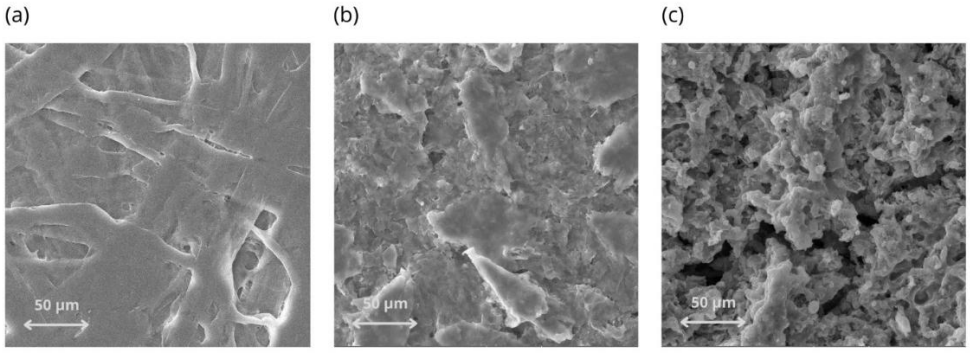

Figure 11: SEM images of cellulose-based substrates: (a) bare cellulose fibers, (b) cellulose coated with GO+AA+Na-Lgs showing a compact and heterogeneous surface, and (c) porous morphology of the GO+AA+Na-Lgs layer after laser carbonization.

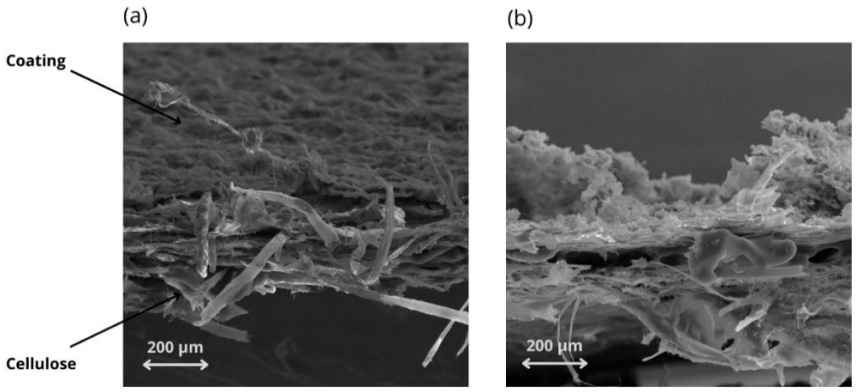

Figure 12: Cross-sectional SEM images of cellulose-based substrates: (a) GO+AA+Na-Lgs coating layer deposited on cellulose, showing distinct interface with fibrous substrate, and (b) structural changes and porosity introduced in the coating layer after laser carbonization.

4.2 Structural Characterization via Raman Spectroscopy and FTIR

Raman spectroscopy was employed to investigate the structure and defect density of cellulose-supported graphene oxide films and composites. For the bare GO coated on cellulose (Figure 13), the spectrum revealed a D band at around 1353 cm^{-1} and a G band at around 1598 cm^{-1}, yielding an ID/IG ratio of 0.765. This comparatively high ratio is characteristic of oxidized GO, indicating that there are numerous oxygenated functional groups, disrupted sp^2 domains, and a generally disordered carbon lattice. Upon reduction of the GO using a laser, the D band shifted slightly to around 1345 cm^{-1} and the G band to around 1591 cm^{-1}, with the ratio increasing slightly to 0.772. Although laser exposure aids the removal of oxygen, the creation of new defects, cracks, and edge sites negates the ordering effect, such that the Raman signature does not reflect an appreciable improvement in structural quality.

Adding ascorbic acid (AA) before laser treatment showed a clear improvement. The GO+AA sample had an ID/IG ratio of 0.753, which is slightly lower than untreated GO. This means that

AA was a good chemical reducer that took away oxygen parts and partly restored sp^2 areas. When this pre-reduced film was treated with a laser, the ratio dropped significantly to 0.519, the lowest of the cellulose-based samples. This big drop in defect density shows that using both chemical and photothermal reduction works well together, creating larger graphitic areas while reducing damage from the laser. This structural change is likely to lead to better conductivity, making Laser GO+AA the best option in the cellulose group.

The incorporation of sodium lignosulfonate (Na-LgS) into the composite mixture had a different effect. The GO+AA+Na-LgS sample exhibited a ratio of 0.807, slightly higher than pristine GO or GO+AA. This indicates that although Na-LgS introduces more carbon content, its partial degradation and crosslinked structure initially introduce more disorder in the carbon structure. Nevertheless, once this composite was subjected to laser treatment, the ID/IG ratio decreased drastically to 0.617, and the G band shifted upward to around 1602 cm^{-1}. These are indicative of the formation of more ordered sp^2 clusters and enhanced graphitization upon heating the lignin-rich film. Though the defect density remained slightly higher than Laser GO+AA, the Na-LgS composite has the additional benefit of improved film thickness, adhesion, and carbon yield following laser carbonization, which can compensate for its slightly higher ratio in overall electrical performance.

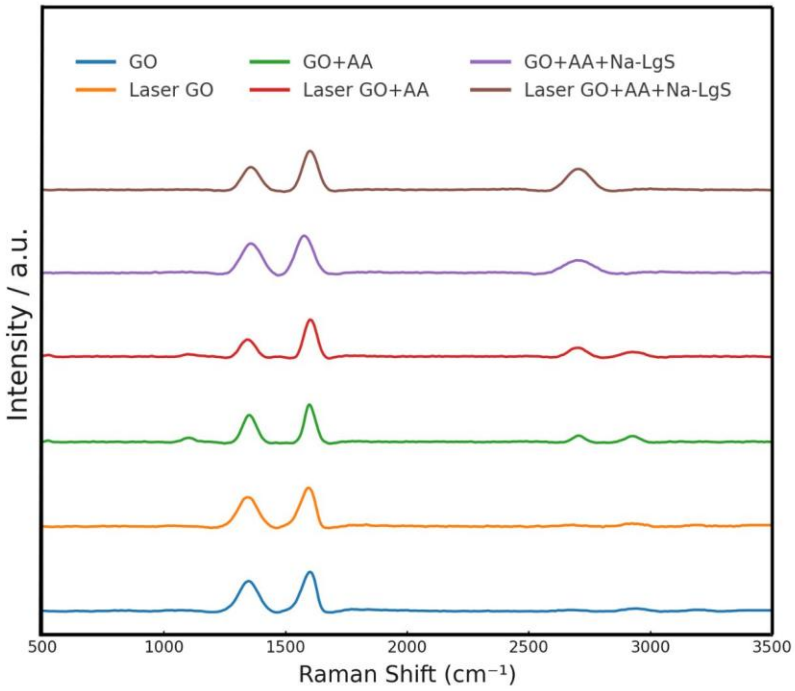

Figure 13: Raman spectra of precursor coatings on cellulose substrates: GO, GO+AA, and GO+AA+Na-Lgs compared with their corresponding laser-carbonized forms. The spectra highlight the emergence of D (~1350 cm $^{-1}$) and G (~1600 cm $^{-1}$) bands, indicating structural disorder and graphitization induced by laser treatment.

4.2.1 FTIR Spectroscopy Analysis

The pure cellulose substrate shows typical absorption bands corresponding to its polysaccharide nature (Figure 14). A broad absorption corresponding near 3400 cm^{-1} is due to the stretching of the O–H bonds arising from inter- and intra-molecular hydrogen bonding. Aliphatic C–H stretching is seen at about 2940 cm^{-1}. The absorption at 1640 cm^{-1} is due to adsorbed water molecules. Strong bands at 1160–1030 cm^{-1} are seen in the fingerprint region due to the stretching of C–O–C and the glucopyranose backbone's C–O stretching. The sharp absorption at about 895 cm^{-1} is due to the β-glycosidic linkage and is a sign of cellulose crystallinity. These peaks are useful and serve as the baseline for chemical changes induced after coating and laser treatment.

When graphene oxide (GO) is deposited, the cellulose spectrum shows new oxygenated functionalities. Primarily evident is the appearance of a C=O stretching band at ~1715 cm^{-1} resulting from the uptake of carboxyl or carbonyl functionalities of GO. The region of O–H stretching (3400 cm^{-1}) is enhanced by the uptake of hydroxyl and epoxide functionalities of GO. There is a sharp C–O stretching feature at about 1240 cm^{-1} evident, confirming the uptake of oxygenated functionalities. All these changes are proof of successful deposition of GO at the cellulose surface.

Laser-treated GO: Upon laser exposure, a distinct reduction of the oxygen functionalities is evident. Intensities of the O–H (3400 cm^{-1}) and C=O (∼1715 cm^{-1}) bands are reduced significantly, and the C–O stretching at 1240 cm^{-1} is dampened. The fingerprint region is made less intense and hence suggests partial decomposition of polysaccharide functionalities and reorganization toward a more conjugated carbon entity. This can be seen as the efficient thermal reduction of GO and is reminiscent of the evolution toward laser-induced graphene (LIG).

When GO is mixed with the known reducing agent, ascorbic acid (AA), the FTIR spectrum is of reduced intensity for oxygenated groups relative to unadulterated GO coatings. The C=O band at ~1715 cm^{-1} is attenuated and the O–H stretch is seen as widened but reduced in intensity, typical of fractional reduction when coating. The C–O stretching feature at 1240 cm^{-1} is still evident but reduced when compared with GO alone.

Laser-treated GO+AA: Laser treatment promotes this reduction additionally. Remaining bands of C=O and C–O nearly disappear and the O–H band is substantially reduced. This laser-treated material spectrum is comparable with that of partially graphitized carbon and possesses cellulose-specific peaks (1160–1030 cm^{-1}) reduced, indicating widespread structural rearrangement. This is

verification of this synergistic effect of AA pre-reduction and laser treatment that leads to the rapid conversion of GO to graphitic regions.

Table 3:FTIR analysis interpretation

Sample	Key Bands (cm^{-1})	Observed Changes	Interpretation
Cellulose	3400 (O–H), 2940 (C–H), 1640 (H–O–H), 1160–1030 (C–O–C, C–O), 895 (β-glycosidic)	Strong cellulose fingerprint, broad O–H stretch	Baseline cellulose structure with characteristic polysaccharide bonds
GO on Cellulose	3400 (O–H), 1715 (C=O), 1240 (C–O), cellulose bands visible	New strong C=O and C–O peaks, more intense O–H	Introduction of oxygenated groups from GO coating
Laser GO	O–H, C=O, C–O strongly reduced	Oxygenated peaks suppressed, fingerprint simplified	Laser-induced reduction and carbonization of GO, forming sp^2-rich domains
GO+AA on Cellulose	3400 (O–H), 1715 (C=O, weak), 1240 (C–O), cellulose peaks	C=O weaker than GO-only, O–H less intense	AA partially reduces GO during coating
Laser GO+AA	Oxygenated peaks nearly absent	O–H, C=O, C–O strongly suppressed	Combined effect of AA reduction and laser processing, leading to more ordered graphitic structure
GO+AA+Na-Lgs on Cellulose	3400 (O–H), 1715 (C=O), 1600 (C=C aromatic), 1180–1210 (S=O), 1030–1050 (S–O)	Additional aromatic and sulfonate peaks	Incorporation of lignosulfonate with GO and AA

Laser GO+AA+Na-Lgs	O–H, C=O, S=O, S–O peaks suppressed	Oxygenated and sulfonate groups eliminated; fingerprint simplified	Laser-induced carbonization removes lignin/GO functionalities, generating conductive sp^2 network

The spectrum of the GO+AA+Na-lignosulfonate coating shows both reduced GO and lignosulfonate additive functionalities. Other than diminished peaks of the oxygenated GOs, new aromatic skeletal absorptions (~1600 cm^{-1}) and sulfonate marker bands (1180–1210 cm^{-1} and 1030–1050 cm^{-1} for S=O and S–O, respectively) are observed, bearing testimony to successful lignosulfonate incorporation within the coating. Even though cellulose backbone peaks remain, though partially shadowed by new functionalities.

GO+AA+Na-Lgs subjected to laser treatment: Following laser treatment, sulfonate and oxygenated peaks are reduced considerably. S=O and S–O bands are significantly reduced, testifying to lignosulfonate group decomposition. At the same time, the peaks of O–H and C=O are reduced, confirming deoxygenation. The fingerprint region is reduced and shows signs of aromatic condensation and sp^2-rich domain formation. This points out laser-induced carbonization of the hybrid coating where both the GO and lignin derivatives play their part toward the fabrication of a conductive network of the LIG.

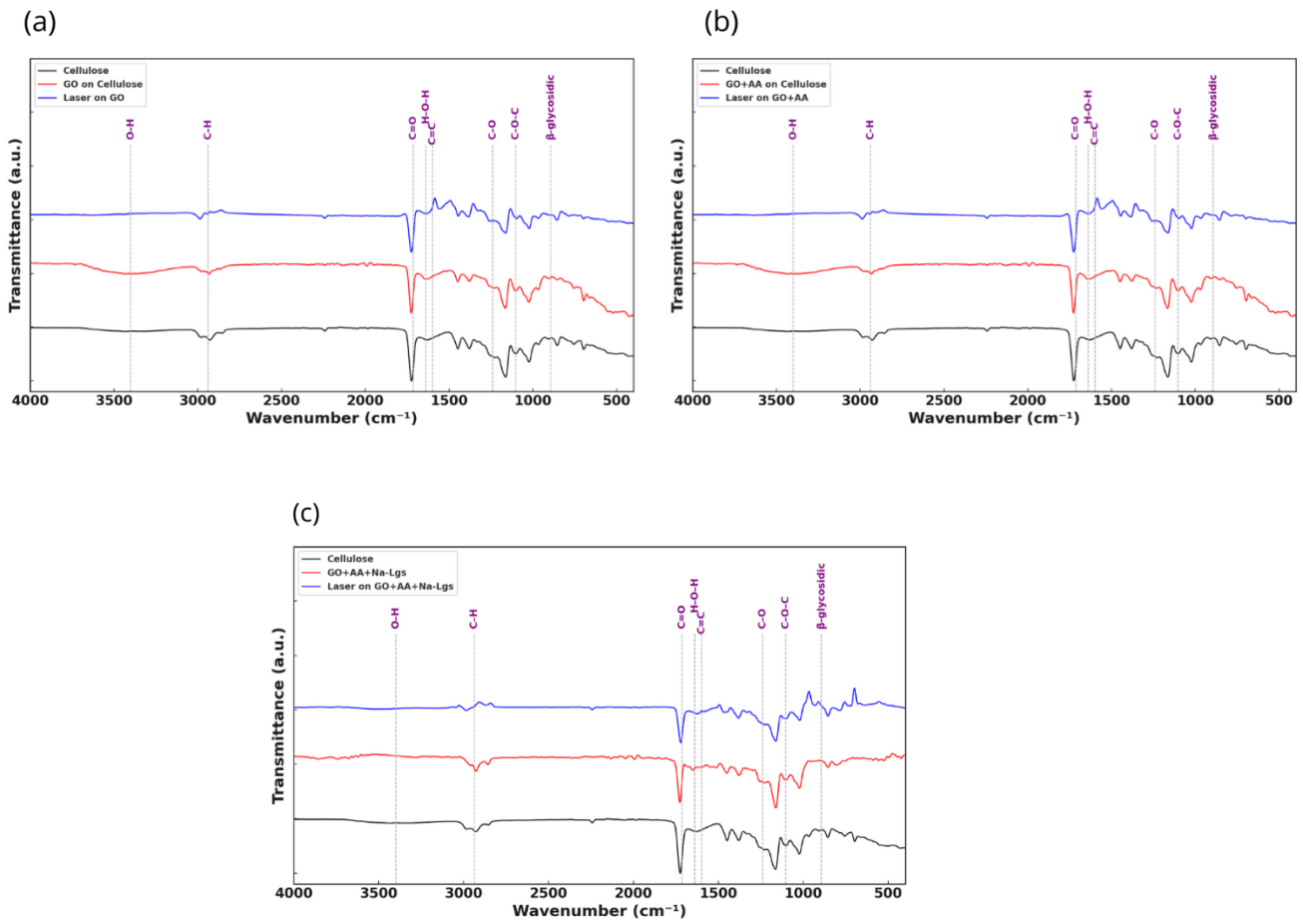

Figure 14: FTIR spectra of cellulose substrate and coated samples: (a) GO and laser-carbonized GO, (b) GO+AA and laser-carbonized GO+AA, and (c) GO+AA+Na-Lgs and laser-carbonized GO+AA+Na-Lgs. The spectra highlight functional groups such as O–H (~3400 cm $^{-1}$), C–H (~2900 cm $^{-1}$), C=O (~1730 cm $^{-1}$), C=C (~1620 cm $^{-1}$), C–O–C (~1050–1150 cm $^{-1}$), and β-glycosidic linkages (~890 cm $^{-1}$). A decrease in oxygen-containing groups after laser treatment confirms partial reduction and graphitization of the coatings.

4.3 Thermal Stability and Decomposition Behaviour via TGA

Thermogravimetric analysis (TGA) was conducted to examine the thermal stability and degradation behaviour of the cellulose samples and their laser-treated versions. The thermal breakdown patterns reveal how the addition of graphene oxide (GO), ascorbic acid (AA), and sodium lignosulfonate (Na-LgS) affects stability, char yield, and the material's overall resistance

to decomposition at elevated temperatures. Figures 15 display weight loss curves for the various systems, whereas the principal parameters, such as onset temperatures, peak derivative values, and residual weights, are listed in Table 3.

4.3.1 Thermal Behaviour of Cellulose

As a reference, pure cellulose paper exhibits the characteristic decomposition behaviour of lignocellulosic fibres (Figure 15, black trace). There is an initial small weight loss below ~100 °C that is attributable to the evaporation of water absorbed from the atmosphere. The primary decomposition process takes place between 300–350 °C, where depolymerization of the cellulose backbone and breakdown of glycosidic bonds occur. An onset peak is seen at ~315 °C, where the steep weight loss (−1.44 %/°C) signifies the rapid degradation of the polymer chains. By 600 °C, merely ~8.9% of the mass is retained as char residue, which reflects the largely volatile composition of cellulose. This low char yield illustrates the necessity of carbon-rich additives to enhance high-temperature properties.

4.3.2 GO on Cellulose Paper

The GO-coated cellulose shows a modified degradation profile compared to pure cellulose (Figure 14-a). Before laser treatment, decomposition begins earlier, with an onset temperature of ~298 °C. This reduction in stability is attributed to the oxygenated functional groups present in GO, which decompose readily to release CO_2, CO, and H_2O. Despite the lower onset, the residue content increases significantly (~13.7%), reflecting the contribution of GO to char formation.

After laser treatment, the onset temperature rises to about 309 °C, suggesting that partial graphitization during laser exposure gives rise to the creation of more thermally stable domains.

However, the residue reduces to about 7.3%. This reduction is due to the consumption or volatilization of loosely held oxygenated carbon fragments within graphene oxide (GO) during laser exposure, leaving behind a thinner carbonized structure. The derivative peak is slightly sharpened (−1.11 %/°C versus −0.90 %/°C), suggesting a more well-defined decomposition event after laser modification. In conclusion, although GO enhances char yield before laser treatment, it provides only modest improvements in stability without further reduction.

4.3.3 GO + Ascorbic Acid on Cellulose Paper

The incorporation of ascorbic acid into GO yields a noticeably different thermal behaviour (Figure 15-b, red and blue traces). Prior to laser treatment, the decomposition onset shifts to a higher temperature (~303 °C), suggesting enhanced stability over GO alone. This is a consequence of the partial reduction of GO by ascorbic acid, which reduces the amount of thermally unstable oxygen groups and encourages closer sheet-to-sheet stacking. The residue (~11.7%) is slightly lower than GO-only, corresponding to the contribution of volatile organic fractions from ascorbic acid.

Interestingly, the derivative peak prior to laser is quite steep (−8.22 %/°C), indicating that decomposition occurs more suddenly. This steep profile indicates concurrent degradation of both the GO sheets and organic additive. Upon laser treatment, however, the profile significantly differs: the onset is moved further upwards (~310 °C), and the degradation rate is slower (−1.09 %/°C). The residue is ~8.5%, which is close to cellulose. These findings verify that laser irradiation stabilizes the carbon layer through the removal of oxygen groups and the creation of graphitic-like domains, thus widening the decomposition window and inhibiting the sudden weight loss seen prior to laser treatment.

4.3.4 GO + Ascorbic Acid + Sodium Lignosulfonate on Cellulose Paper

The GO+AA+Na-LgS system has the most visible thermal signature (Figure 15-c). Before exposure to the laser, decomposition is initiated at a lower temperature (~290 °C) than the other samples. The reason for this is the fact that lignosulfonate contains sulfonate groups that are prone to thermal degradation and decompose at relatively lower temperatures. Despite the premature onset, the sample leaves a very high char residue (~42.3%). Such a high residue is consistent with the aromatic, cross-linked structure typical of lignin derivatives, which tend to carbonize instead of volatilizing. The derivative peak is −1.52 %/°C and indicates moderate degradation over a very wide temperature range.

Following laser carbonization, the onset is slightly higher (~297 °C), indicating some stabilization of the carbonized structure. The residue is still very high (~30.6%), indicating that lignosulfonate significantly increases char yield. The derivative peak is less intense (−0.74 %/°C), corresponding to a broader and more gradual decomposition process. This suggests that the laser-treated sample is more resistant to sudden degradation, in agreement with the thicker, lignin-rich carbonized band seen via SEM.

Table 4: TGA/DTG results of cellulose-based samples under N_2 atmosphere.

Sample	Residue (%)	Peak onset point (°C)	Peak Derivatives (%/°C)
Cellulose paper (bare)	8.86	314.63	-1.45
GO on Cellulose (pre-laser)	13.68	297.73	-0.90
GO on Cellulose (post-laser)	7.28	308.64	-1.117
GO+AA on Cellulose (pre-laser)	11.69	302.54	-8.223

GO+AA on Cellulose (post-laser)	8.48	309.63	-1.09
GO+AA+Na-LgS on Cellulose (pre-laser)	42.25	290.47	-1.521
GO+AA+Na-LgS on Cellulose (post-laser)	30.56	296.64	-0.74

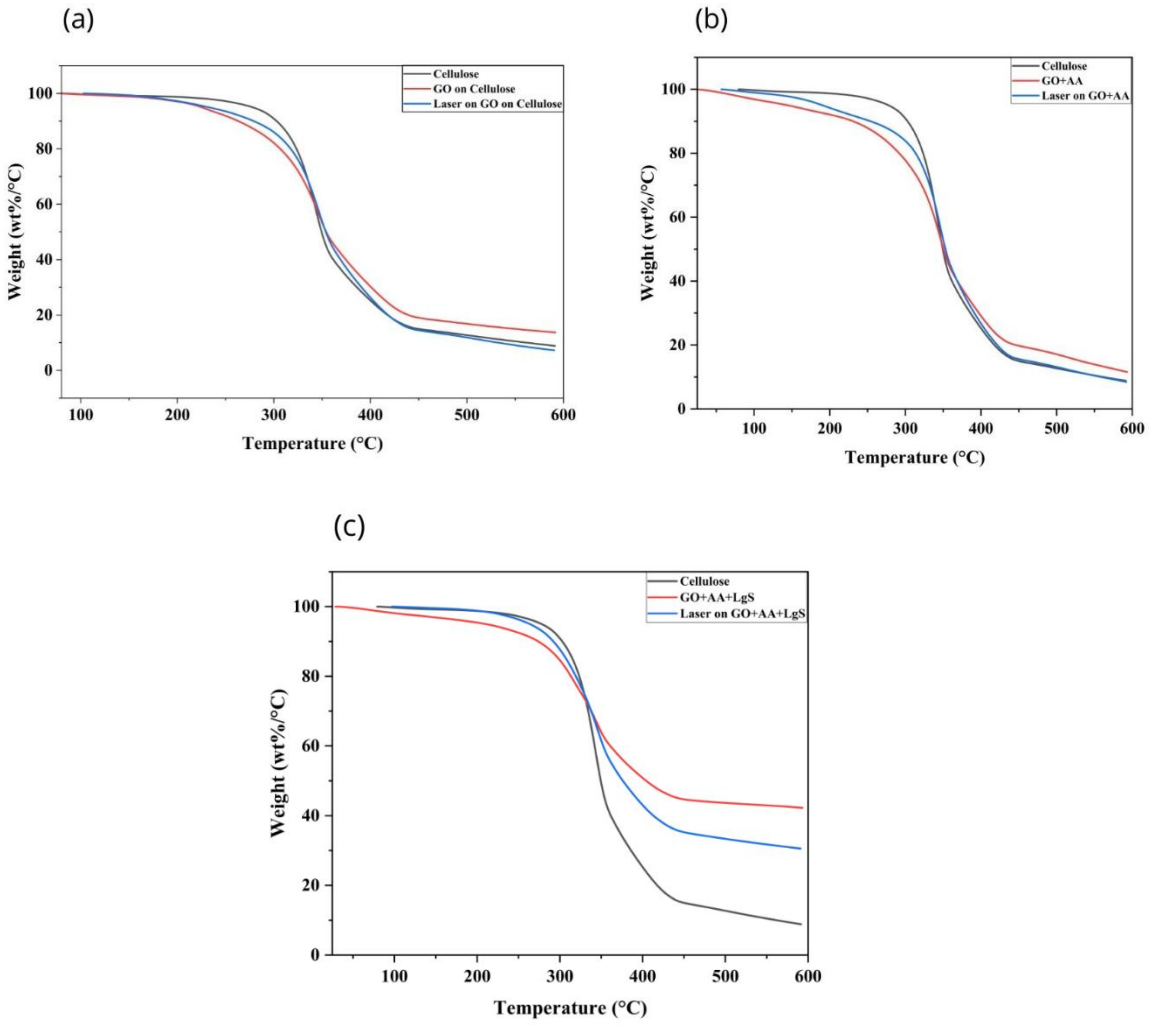

Figure 15: Thermogravimetric analysis (TGA) of cellulose substrates and coated films: (a) GO and laser-carbonized GO on cellulose, (b) GO+AA and laser-carbonized GO+AA, and (c) GO+AA+Na-Lgs and laser-carbonized GO+AA+Na-Lgs. The weight loss curves highlight major thermal degradation steps, including initial moisture loss below ~150 °C, primary

cellulose and coating decomposition between ~250–380 °C, and residual char yield above 400 °C, with laser-carbonized samples showing higher stability due to partial graphitization.

4.4 Electrical Conductivity and Sheet Resistance Measurements

The sheet resistance of the laser carbonized films was measured using a standard four-point probe technique to minimize contact resistance errors. Sheet resistance applies to two-dimensional systems, including thin films. The regular resistance for a 3D shape can be expressed as:

(Eq. 4.1) $$R = \rho \frac{L}{A} = \rho \frac{L}{Wt}$$

Where ρ is the resistivity of material (depends on material and not geometry), L is the length and A is the cross-section area. W is the width and t is the thickness.

The sheet resistance (Rs) is also defined as resistivity per thickness and can be expressed as:

(Eq. 4.2) $$R = R_s \frac{L}{W}$$

Sheet resistance refers to uniform sheet thickness measured in Ω/□ (ohms per square). Sheet resistance is defined as the resistance of a single square unit of film. When the width and length of the measured area are identical (W = L), sheet resistance is equal to normal resistance ($R = Rs$).

Two-point and four-point probe tests are commonly used to assess sheet resistance. Figure 16 shows a four-point probe instrument. Four-point probe measurement involves injecting current with one pair of probes and measuring voltage with the other pair, unlike traditional two-point resistance measurements. When no current passes through the sensing probe, the instrument

detects the voltage across the resistance and eliminates errors caused by test leads and contact resistance.

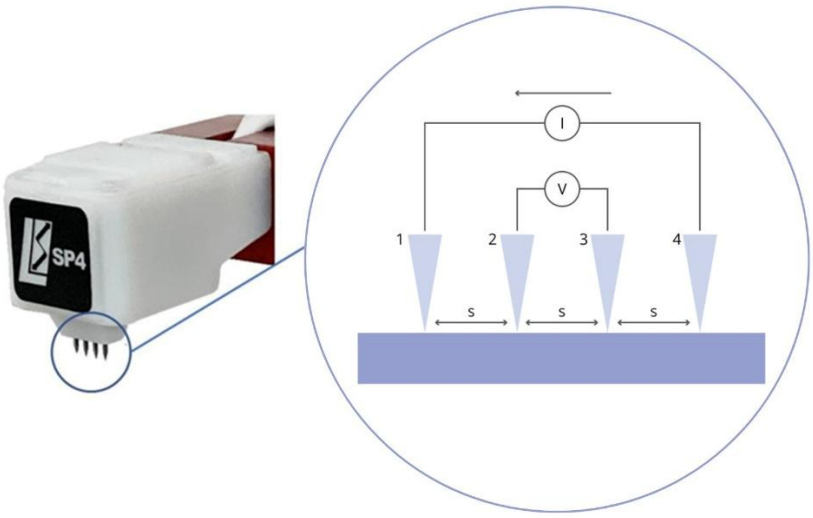

Figure 16: Four-point probe device and working diagram, in which one pair creates a current(Outer Probes) in the material while the other pair measures the voltage (Inner Probes).

Equation 4.2 may be used to determine the sheet resistance of a film using a two-point probe. This approach measures the resistance (R) between the sample's two ends.

A Digital Multimeter (DMM) is used to produce current and measure voltage. According to Smits [65], the V-I plot should be linear with a slope of $\ln(2)/\pi\ Rs$ for film thickness less than half of probe spacing and lateral dimensions 40 times larger than probe spacing, where $\ln(2)/\pi = 4.53$. A plot of measured voltage against injected current is used to determine the sheet resistance.

For the four-point probe the sheet resistance can then be calculated using the following equation:

(Eq.4.3)
$$Rs = \frac{\pi}{\ln(2)} \frac{\Delta V}{I} = 4.53236 \frac{\Delta V}{I}$$

The equation for sheet resistance works well only if the sample is much larger (about 40 times bigger) than the spacing between the probes (s= 1.25mm), and if the sample is thinner than 40% of that spacing. If these conditions are not met, the edges of the sample get in the way and limit the current flow, which makes the sheet resistance seem higher than it really is. To fix this, a correction factor that depends on the shape and size of the sample needs to be multiplied to the measured sheet resistance (Eq. 4.3).

For rectangular samples, calculating the correction factor is more complex because there isn't a simple formula. Instead, we use a table of correction factors based on experimental data [108]. These values only work when the probes touch the sample at its centre and are lined up parallel to the longest edge of the rectangle.

The electrical conductivity (σ) of the films was approximated from the resistance values based on the measured samples geometric parameters. The conductivity is the inverse of resistivity (ρ) and can be represented as:

$$\sigma = \frac{1}{\rho} = \frac{L}{R \cdot A}$$

where R is the measured resistance (Ω), L is the distance between the electrodes (m), and A is the cross-sectional area of the conducting path (m^2).

For thin-film samples, such as the coated cellulose substrates used in this study, conductivity is more conveniently calculated using the measured sheet resistance (Rs and film thickness (t):

$$\sigma = \frac{1}{R_s \cdot t}$$

Here, Rs is the sheet resistance expressed in Ω/sq, and t is the average film thickness in meters. This formulation allows for an accurate evaluation of electrical transport properties without the need to directly measure bulk dimensions, which can be challenging for thin and flexible films.

4.5 Laser Parameter Optimization

To investigate the electrical properties of the laser-patterned composite materials, films with an average thickness of 25μm were prepared and laser-treated. A range of different laser parameters (i.e., incident laser power and scanning speed) were tested to pattern sample lines (10×4 mm) on the primary films for sheet resistance measurement. A systematic study of laser parameters particularly **power** and **scan speed** were conducted to optimize electrical performance. It was found that moderate and medium scan speeds produced the most conductive films. Too low a power resulted in insufficient carbonization, while too high a power caused surface ablation or delamination. This balance is critical in tuning film properties for application in disposable RFID systems and transient electronics.

In our case the length, width and thickness of the laser carbonized part is l= 10mm, w= 4mm and t= *20μm.* A correction factor needs to be applied to the measured sheet resistance (Eq. 4.3). According to the experimental data [108] the correction factor based on our geometry is 0.5957.

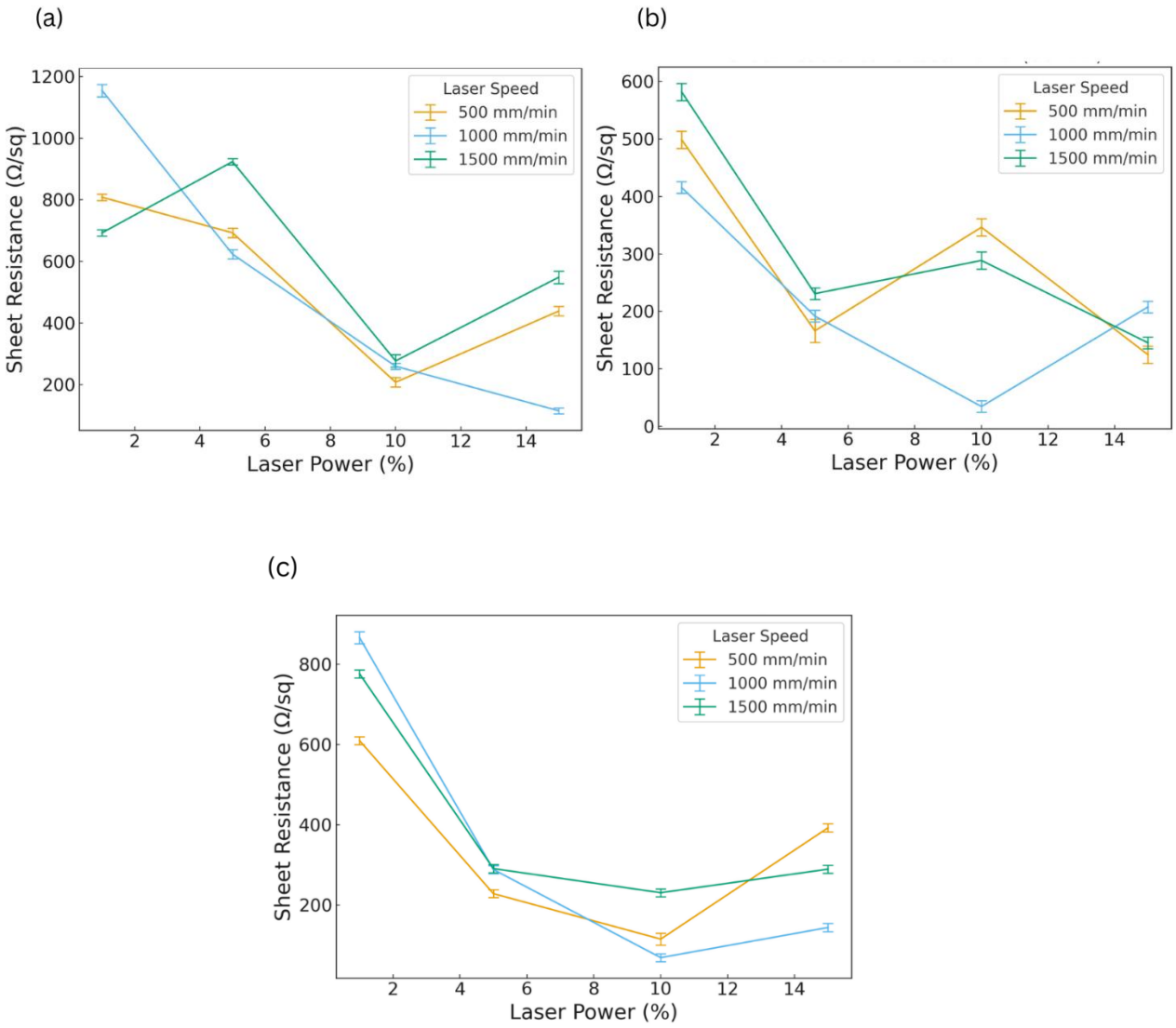

Figure 17: Sheet Resistance comparison of all the samples at different Laser Power and scanning speed (a)Go coated on Cellulose, (b) GO+AA coated on cellulose and (c) GO+AA+Na-Lgs Coated on cellulose

Figure17 shows the sheet resistance of all the samples at different levels of speed and power of the laser. Table 5 presents the comparison of resistance, sheet resistance, laser parameters, and calculated electrical conductivity for the three cellulose-based films.

Table 5:Electrical Properties of the cellulose-based samples.

S.No.	Coating	Resistance (Ω)	Sheet Resistance (Ω/□)	Laser Power (%)	Laser Speed (mm/min)	Conductivity (S/m)
1	GO	50	115.5	15	1000	4.33×10^{2}
2	GO+AA	15	34.6	10	1000	3.62×10^{3}
3	GO+ Na-Lgs-AA	30	69	10	1000	7.25×10^{2}

The first sample, coated with only GO, exhibited a sheet resistance of 115.5 Ω/sq and correspondingly a conductivity of 4.33×10^{2} S/m. The second sample, where GO was reduced with ascorbic acid (GO+AA), showed a much lower sheet resistance of 34.6 Ω/sq, resulting in the highest conductivity value of 3.62×10^{3} S/m. This clearly demonstrates the effectiveness of ascorbic acid in enhancing the reduction of graphene oxide and improving the formation of conductive pathways. The third sample, prepared with GO, ascorbic acid, and sodium lignosulfonate (GO+Na-Lgs-AA), exhibited an intermediate performance with a sheet resistance of 69 Ω/sq, yielding a conductivity of 7.25×10^{2} S/m.

4.6 Comparison with Literature

Laser carbonization of a variety of organic, polymeric, and bio-based materials has been the subject of several studies [66–68]. When compared to other carbonization techniques like thermal and chemical, laser carbonization, also known as laser graphitization, has been shown to be a quick, precise, flexible, and adjustable way to carbonize materials [69]. Nevertheless, all the benefits, the laser type, its settings, the precursor, and the surrounding environment all have a significant impact on the electrical characteristics and degree of carbonization that are achieved. Achieving high electrical conductivity is difficult for several reasons because of this intricacy. Researchers have used either costly and complex materials like gold plating [45] or intricate laser settings like gas-

filled chamber [70] to overcome this difficulty and get a high electrical conductivity. This work shows comparable sheet resistances while keeping the material and manufacturing process simple when compared to the highly referenced works displayed in Figure 18. (References used in the figure are the LIG produced on the samples with the coatings)

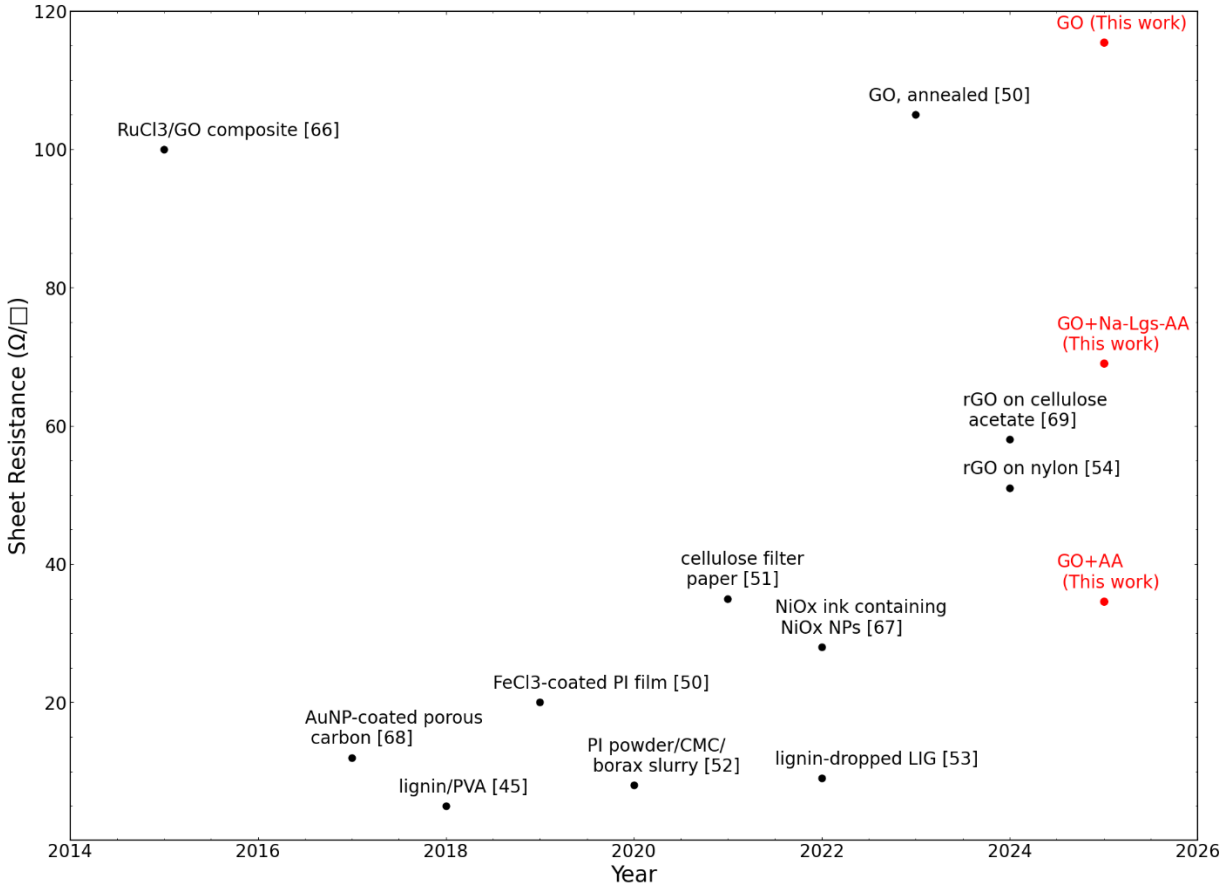

Figure 18: Comparing sheet resistance that is achieved in this work with literature.

Chapter 5: Compressible Flow Exfoliated Graphene

5.1 Overview of Compressible Flow Exfoliation (CFE)

Graphene has broadly gained popularity as an ideal candidate for next-generation electronics, sensors, and energy devices given the excellent combination of electrical conductivity, mechanical strength, and elasticity [70]. However, large-volume, low-cost production of graphene is still challenging. Traditional methods like chemical vapor deposition (CVD), mechanical exfoliation, and chemical oxidation–reduction possess low yield with high-quality graphene output (e.g., CVD) or high defect density as well as contamination (e.g., chemical reduction in graphene oxide).

Compressible Flow Exfoliation (CFE) is scalable, environmentally friendly, low-cost method for the production of few-layer graphene from large amounts of bulk graphite. The mechanism of CFE is based on the removal of a graphite dispersion through a constricted orifice under conditions of high pressure as well as compressible flow. Due to the sudden expansion and turbulence of the fluid, the resultant shear stresses, cavitation phenomenon, as well as pressure gradients, are capable of breaking through the weak van der Waal forces that are responsible for holding back the graphene sheets together [72]. The outcome is the delamination of the graphite into thin flakes of graphene in the solvent medium.

An important advantage that CFE has over applying chemical methods is that in preparing defect-reduced graphene, no powerful oxidants or reductants are needed to therefore preserve the native sp^2 bonding network. Secondly, when comparing to ultrasonication exfoliation, CFE has the upper hand in terms of scalability as well as energy efficiency, by applying continuous treatment in large volumes of dispersion [67]. It has been demonstrated that flow pressure, nozzle shape, solvent

content, and temperature significantly affect exfoliation yield, flake size, and defect density. The exfoliated products are commonly collected through centrifugation to eliminate unexfoliated graphite and yield stable dispersions of graphene. These dispersions can thereafter be employed in direct use for the purpose of coating, printing, or composite preparation, rendering CFE very promising for application in flexible electronics, supercapacitors, as well as in coatings.

5.2 Preparation and Deposition of CFE-Graphene Films on PET

5.2.1 Preparation of CFE-graphene dispersion

The Compressible Flow Exfoliation (CFE) technique was applied to prepare the graphene from the delamination of the graphite into few-layer graphene in compressible flow. A binary solvent solution consisting of **deionized (DI) water** and **isopropanol (IPA)** was used to exfoliate the dispersion of the graphite powder. The solvent choice is commonly seen in works involving liquid-phase exfoliation, as IPA/water's combined surface energy is similar to that of graphene, thus aiding exfoliation while enhancing suspension stability.

The exfoliation process was carried out in-house in a proprietary CFE equipment. Due to the protection of intellectual property, we cannot provide detailed operating parameters like nozzle structure, flow rates, pressure/temperature regimes. The overall process consists of flowing the solvent–graphite mixture through high-pressure, compressible flow regimes where mechanical energy from applied shear stresses, turbulent vortices, as well as cavitation events, is imparted to tear apart weak van der Waals bonding between neighbouring graphene sheets to produce few-layer graphene sheets.

The resultant dispersion was then characterized to find the concentration of the graphene. Gravimetric analysis was done by evaporating to constant weight a known volume from the dispersion and noting the mass of the recovered graphene. Through this, the concentration of exfoliated graphene in the suspension was estimated to be **0.15 g/L**.

The quality of graphene produced via CFE is highly dependent on the selection of solvents and the control of exfoliation parameters. These parameters were chosen based on prior studies showing that moderate sonication and appropriate solvent stabilization result in high-quality few-layer graphene dispersions [67].

Additionally, the optimization of the exfoliation process contributes to the development of scalable methods for graphene production, which is crucial for commercializing graphene-based technologies. CFE, with its relatively simple setup and scalability, offers a promising alternative to traditional graphene production methods such as chemical vapor deposition (CVD) and chemical reduction of graphene oxide, which are more costly and energy intensive [68]. As the demand for graphene continues to rise in fields such as flexible electronics, energy storage, and sensors, the need for cost-effective and scalable methods of production will only grow. Compressible Flow exfoliation, especially when optimized through solvent choice, sonication power, and centrifugation, offers a viable path to meeting this demand while maintaining high-quality graphene.

5.2.2 Formulation into ink and deposition on PET

The exfoliated graphene dispersion thus obtained through compressible flow exfoliation (CFE) was then formulated into an ink suitable for film coating. As pristine graphene dispersions are

generally low in viscosity in their natural state as well as possess low film-forming capacity, 1 wt% carboxymethyl cellulose (CMC) was added to the solution. The CMC added to the solution played two primary roles: (i) that of a rheology modifier to increase the viscosity of the dispersion to facilitate controlled spreading of the ink in the process of coating; and (ii) that of a binder to improve attachment between the substrate and the graphene flakes to facilitate forming stable crack-free films. CMC is commonly applied in printed as well as coated electronics due to its capacity to hinder particles from settling as well as aid in uniform film forming, rendering it an ideal additive in solution-processed coatings from graphene.

From this CFE dispersion, 50 mL was taken and in a separate beaker, 50 mL of deionized (DI) water containing 1 wt% CMC was prepared (Figure 19). Both solutions were then combined under proper mixing conditions, giving a total of 100 mL of graphene ink. The initial CFE graphene dispersion had a concentration of 0.15 g/L, as determined by gravimetric analysis. After mixing, the effective graphene concentration in the final ink was reduced to 0.075 g/L.

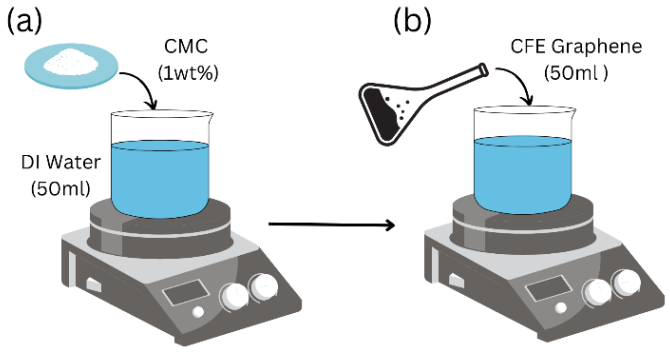

Figure 19: Preparation of CFE graphene dispersion: (a) dissolution of 1 wt% carboxymethyl cellulose (CMC) in 50 mL deionized water under stirring, and (b) addition of 50 mL CFE graphene suspension to the prepared CMC solution.

The prepared graphene-CMC ink was then deposited onto polyethylene terephthalate (PET) substrates using the doctor-blade coating technique. PET was selected due to its favourable combination of flexibility, transparency, and mechanical robustness, which make it a widely used substrate in flexible and transient electronics. Prior to coating, the PET sheets were cleaned with ethanol and deionized water to remove surface contaminants that could interfere with film adhesion. The graphene–CMC ink was deposited employing a doctor blade that casts the dispersion in a controlled gap thickness on the PET substrate. A multi-layer film-coating approach was employed, whereby the deposition plus drying cycle was repeated to deposit ten layers in all. Each layer was dried under mild heating conditions prior to the next coating step to ensure solvent removal and consolidation of the film.

The same film preparation technique was used here as in the cellulose substrates discussed above in this thesis, to obtain consistency in the approach to film-coating as well as to enable substantial comparison among different substrates.

For coating, a total of **6 mL of this prepared ink** was used to cover a **7 × 8 cm² (56 cm²)** PET sheet. The 6 mL of ink contained about **0.45 mg of graphene in total**. Since this mass was distributed evenly over the 56 cm² sheet, the **graphene loading per unit area was around 0.008 mg/cm² (or 8 µg/cm²)**. After drying, the **thickness** of the final multilayer film was measured to be about **10±1µm**.

5.3 Laser Carbonization Process and Sheet Resistance Measurement

Coated PET films from CFE-graphene inks were carbonized using blue-laser to enhance conductivity by localized synthesis of laser-induced graphene (LIG). A systematic study was

carried out to obtain the best conductivity by varying the power of the laser (30%, 50%, 80%, 100%) as well as the scan speed (500, 1000, 1500 mm/min) with all other parameters kept constant.

The four-point probe technique was employed to determine the sheet resistance (Ω/sq) of the laser-carbonized films. The findings (Figure 20) show significant sheet resistance dependence on both the power of the lasers as well as the speed of the scans. Low power from the lasers (30%) resulted in fairly high sheet resistance values between 40–60 Ω/sq, due to insufficient carbonization as well as low connectivity among the graphene flakes. An increase in the power from the lasers to 50% decreased the resistance considerably (22–35 Ω/sq), suggesting improved graphitization.

The best performance was observed at **80% power and 500 mm/min**, where the sheet resistance reached to **16.17 Ω/sq**. This optimum can be attributed to a balance between sufficient laser energy to induce graphitization and controlled heating that prevented over-burning of the substrate. When the scan speed was increased to 1000 or 1500 mm/min at the same power, the sheet resistance increased again (15–10 Ω/sq), as the reduced dwell time of the laser provided less energy per unit area. At maximum power setting (100%), sheet resistance rose again (12–28 Ω/sq), perhaps because localized overheating resulted in partial evaporation of the conductive layer and destruction of the graphene network. These findings confirm that under- as well as over-exposure of the laser is destructive to conductivity, and that optimal processing conditions are required in order to achieve minimum sheet resistance.

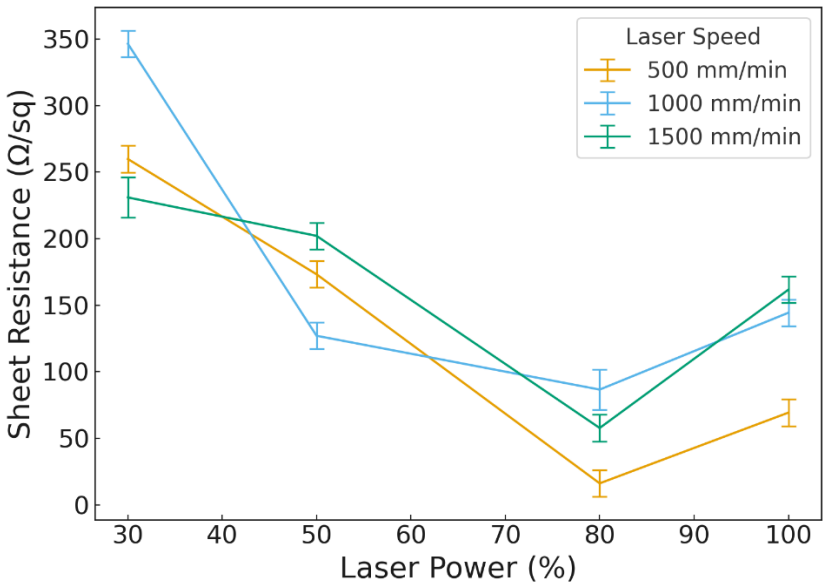

Figure 20: Sheet Resistance comparison of the CFE Graphene coated on PET at different Laser power and Scanning Speed.

Overall, the study established that laser power and scan speed are critical parameters in tuning the conductivity of PET-based CFE graphene films. The optimized condition (80% power, 500 mm/min) produced a sheet resistance of 16.17 Ω/sq, which is among the lowest values reported for laser-carbonized films on polymer substrates, highlighting the suitability of this approach for flexible and transient electronic applications.

5.4 Characterization of CFE-Graphene Films

A detailed characterization of the CFE-graphene films deposited on PET substrates was conducted to gain insight into the effect of laser carbonization on their structure, morphology, chemical, and thermal behaviour. Given that their performance in electronic applications is critically dependent on both their microstructure as well as their stability, several complementary techniques were conducted. SEM was utilized to examine surface morphological features as well as microstructural change following laser treatment, whereas Raman spectroscopy was used to gain information on

graphitization extent and defect density. FTIR spectroscopy was utilized in order to recognize functionalities to assess chemical conversions throughout carbonization, whereas TGA was conducted in order to assess thermal stability and film's thermal breakdown behaviour. Collectively, these methodologies offered an entire assessment of the CFE-graphene films, allowing for definite separation between non-carbonized coatings as well as between laser-carbonized regions of the graphene.

5.4.1. Scanning Electron Microscopy (SEM) Analysis

The cross-sectional and surface morphology of the films were characterized by SEM and are depicted in Figure 19. From these pictures, the significant changes in the PET substrate after CFE-graphene coating and after laser carbonization are clearly illustrated.

The uncoated PET substrate (Figure 21-a) is very flat in appearance and smooth looking. There are no flakes or pores to observe, characteristic for uncoated PET. This smooth looking flat surface is significant, as this guarantees any observed change after laser treatment is purely due to the CFE-graphene coat and not from the substrate.

Once coated with CFE-graphene ink (Figure 21-b), the PET surface became more textured and rough. A continuous thin film appeared throughout the substrate. The flakes were coated in a uniform manner because of the doctor-blade coating technique, though under this magnification the separate sheets of the graphene are not individually resolved. This indicates that the coating process was satisfactory and formed a uniform precursor film prior to laser treatment.

When coated PET is exposed to the blue carbonization laser (Figure 21-c), the surface was intensely altered. What was previously smooth, dense film was transformed into a porous structure

that is similar to foam. This is characteristic of laser-induced graphene (LIG) and is due to the rapid heating of the surface by the high-energy laser, expelling gases as well as breaking the binder. The remaining carbon reorganizes into sp^2-bonded graphene domains. The porous texture creates a larger surface area and allows the flakes to connect more effectively, which explains the very low sheet resistance (as low as 2.8 Ω/sq) measured in these films. The cross-sectional SEM images provide additional confirmation of these changes. The cross-section of pristine PET (Figure 20-a) shows only a uniform polymer surface without any added layers. In contrast, the laser-carbonized CFE-graphene on PET (Figure 22-b) clearly shows a separate top layer formed above the PET substrate. This top layer corresponds to the laser-carbonized graphene film and appears more porous and rougher compared to the smooth PET underneath. Importantly, the PET itself remains intact, which proves that the laser only modifies the coated layer without damaging the polymer support.

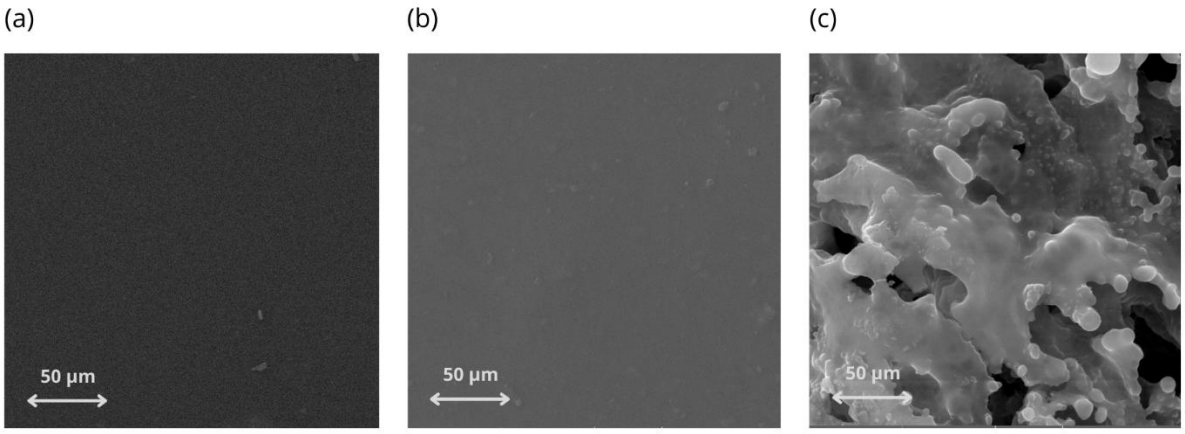

Figure 21: SEM images of PET-based substrates: (a) pristine PET surface, showing smooth morphology, (b) PET coated with CFE graphene, forming a uniform thin film, and (c) laser-carbonized CFE graphene coating, displaying a highly porous and wrinkled structure as a result of laser-induced graphitization.

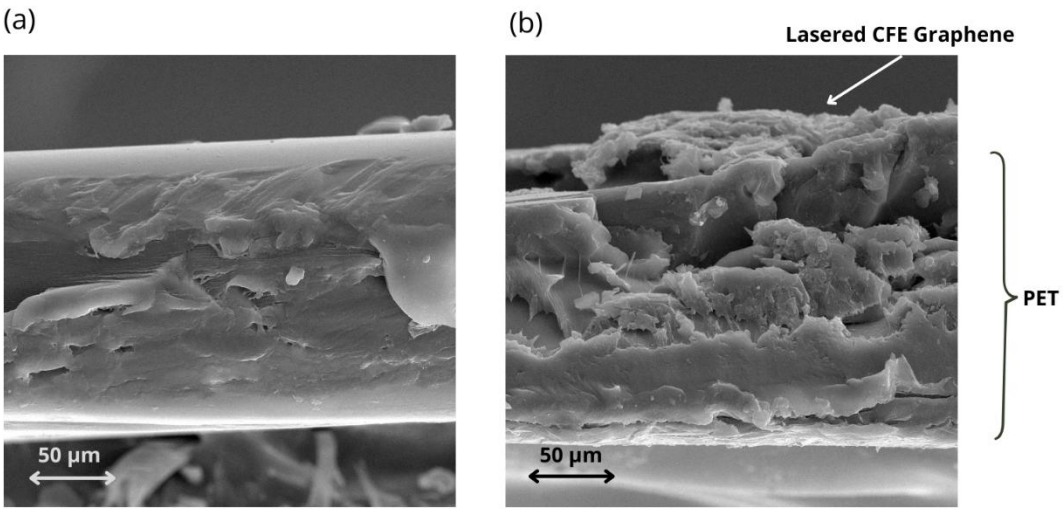

Figure 22: Cross-sectional SEM images of PET substrates: (a) pristine PET, showing smooth cross-sectional morphology, and (b) PET with laser-carbonized CFE graphene coating, highlighting a distinct layered interface and porous structure induced by laser treatment.

5.4.2. Raman Spectroscopy Analysis

Raman spectroscopy was used to study the structural evolution of CFE graphene films before and after laser carbonization on PET substrates. For the untreated CFE graphene film (Figure 23-b), the Raman spectrum showed a weak D band at 1301.8 cm^{-1} and a G band at 1614.2 cm^{-1}, with an I_D/I_G ratio of 0.252. Such a low value indicates that the sp^2 domains are relatively intact with fewer defects; however, the corresponding 2D band was weak and broad at ~2908 cm^{-1}, with an I_{2D}/I_G ratio of only ~0.19. This suggests that, despite having fewer defects, the material lacked sufficient graphitic ordering and continuous π–π conjugation. In other words, the carbon was not yet reorganized into an extended conductive graphene network.

Following laser treatment, significant changes were observed. The D band shifted to 1336.5 cm^{-1}, while the G band became observable at 1577.6 cm^{-1}, with the I_D/I_G ratio raising to 0.561. This

higher ratio implies an increase in disorder; however, in the context of laser-induced graphene, it reflects the creation of numerous edges, pores, and defect sites that accompany localized ablation and carbonization. These structure modifications that increase the surface area also provide interconnectivity across the network in the graphene. Emergence of a sharper 2D band at ~2677 cm^{-1}, with an I_{2D}/I_G ratio of ~0.49, again confirms desired multilayer graphene-like domain creation as well as extensive sp^2 ordering. Taken together, the transition from a low I_D/I_G with weak graphitic features (CFE only) to a higher I_D/I_G with a strong 2D band (Laser-CFE) demonstrates that laser irradiation transforms the precursor into a porous, edge-rich, and electrically conductive laser-induced graphene (LIG) network. While defects increased, they are not unfavourable; instead, they are essential for producing a highly conductive and application-ready carbon architecture. This structural evolution underpins the improved electrical performance of the films and validates laser processing as a critical step in fabricating transient, graphene-based electronics.

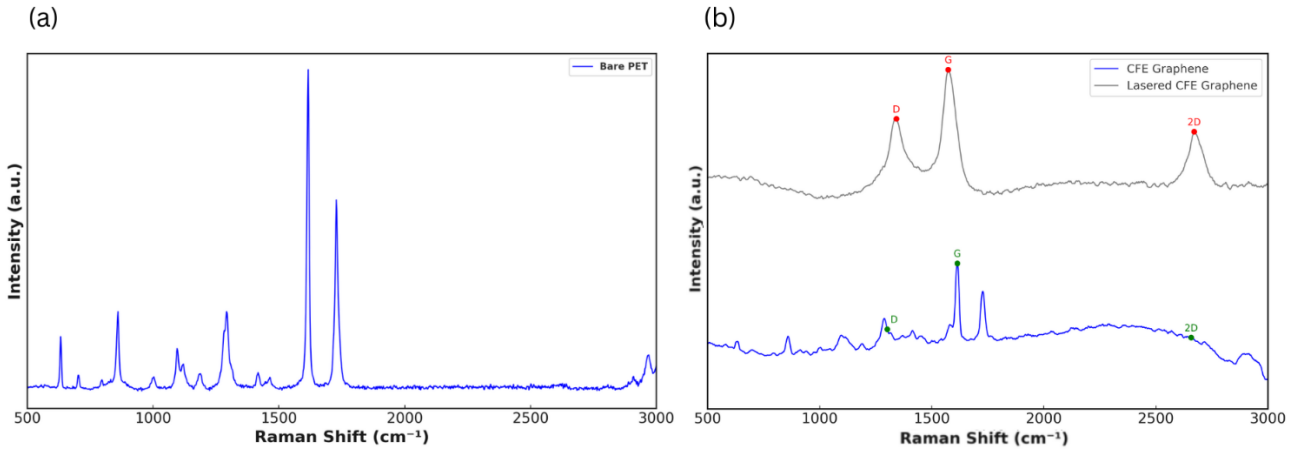

Figure 23: Raman spectra of PET and CFE graphene-coated PET: (a) pristine PET sheet exhibiting polymer-related peaks, and (b) CFE graphene coating before and after laser carbonization. The lasered sample shows the appearance of prominent D (~1350 cm^{-1}), G (~1580 cm^{-1}), and 2D (~2700 cm^{-1}) bands, confirming the formation of graphitic domains and partial structural ordering after laser treatment.

5.4.3. Fourier Transform Infrared (FTIR) Spectroscopy Analysis

The pure PET film displays its usual peaks: a prominent C=O peak at ~1720 cm^{-1}, aromatic C=C bands at about 1600 cm^{-1}, C–O–C stretching at 1250 cm^{-1}, and other oxy peaks at about 1100 cm^{-1}. These are the fingerprint bands of PET, and they remain unaltered in all the samples, indicating that PET itself is not being destroyed by coating or laser treatment (Figure 24).

When the PET is coated with CFE (pre-laser), new peaks arise. There is a strong band at around 3400 cm^{-1} suggestive of O–H groups, and extra peaks of C=O (around 1720 cm^{-1}) and of C–O (1250–1100 cm^{-1}) are evident and are caused by the oxygen-containing groups of the CFE coating. This is evidence of the surface of the CFE coating containing many oxygen functional groups.

Table 6: FTIR Interpretation

Sample	Main Peaks (cm^{-1})	Interpretation
Bare PET	1720 (C=O), 1600 (C=C), 1250 (C–O–C), 1105 (C–O)	Normal PET structure; stable reference
CFE on PET	3400 (O–H), 1720 (C=O), 1250–1100 (C–O/C–O–C)	CFE coating adds oxygen functional groups
Laser–CFE on PET	1600 (C=C), weak O–H/C=O/C–O bands	Laser removes oxygen groups, leaving graphitic sp^2 carbon; PET still intact

Subsequent laser carbonization of the CFE coating makes these bands of oxygen-related stretching (O–H, C=O, C–O) significantly weaker, indicating that the laser etches out the oxygen groups and thins the coating. Meanwhile, the C=C band at about 1600 cm^{-1} is preserved, consistent with the laser transforming the coating into a more graphitic sp^2-rich phase. Since the peaks of the PET are unaltered, the substrate is unaltered and only the coating is chemically altered.

Overall, it is verified by FTIR that laser treatment transforms the CFE coating from an oxygen-rich coating into a graphitic laser-induced graphene (LIG) film while leaving the PET intact.

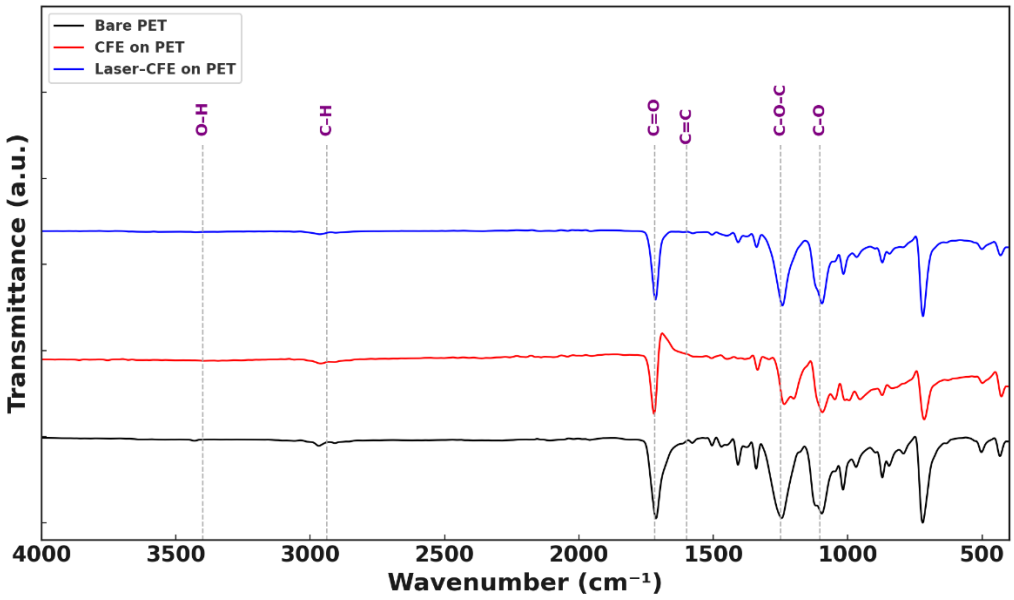

Figure 24: FTIR spectra of PET-based samples: bare PET, CFE graphene-coated PET, and laser-carbonized CFE graphene on PET, showing characteristic peaks corresponding to O–H, C–H, C=O, C=C, C–O–C, and C–O groups. The reduction in oxygen-containing functional groups after laser treatment indicates partial graphitization of the CFE graphene coating.

5.4.4. Thermogravimetric Analysis (TGA)

The results of TGA yield a clear indication of the effect of the CFE graphene coating on the thermal stability of the PET substrate. Thermal degradation of the bare PET sheet is initiated at about 391.43 °C, which is characteristic of PET, since its polymer main chains are volatilize at higher temperature (Table 7). The highest degradation is observed with peak derivative of –2.08%/°C, and at the completion of the heating cycle, only 7.75% of the residue is left behind, affirming nearly complete disruption of the polymer matrix.

Table 7: TGA/DTG results of PET and CFE graphene samples.

Sample	Residue (%)	Peak onset point (°C)	Peak Derivatives (%/°C)
PET	7.75	391.43	-2.08
CFE Graphene on PET	13.10	393.67	-2.09

When the PET is coated with CFE graphene, its behaviour changes noticeably (Figure 25). The onset of degradation shifts slightly higher to 393.67 °C, and although the peak degradation rate remains similar (–2.09%/°C), the residue content increases significantly to 13.10%. This difference highlights the role of the graphene coating as an effective protective film barrier. The presence of the CFE graphene layer prevents rapid volatilization of the polymer chains by restricting mass transport of gaseous degradation products and by reducing oxygen and heat penetration into the bulk of the PET substrate. In other words, the graphene sheet acts as a shield that slows down the decomposition process and forces a portion of the PET to stabilize in the form of carbonaceous char rather than being completely lost as volatiles.

The increased char yield of the graphene-coated PET is a strong indicator of this barrier effect. Not only does the graphene coating slow the start of decomposition, it facilitates the development of a stable protective layer when heated. This residual layer of carbonized material enhances the general structural integrity of the film after extensive thermal exposure. This kind of thermal stability is very useful when it comes to flexible and transient electronics applications where materials end up being subjected to local heating when operating these devices or processing using laser.

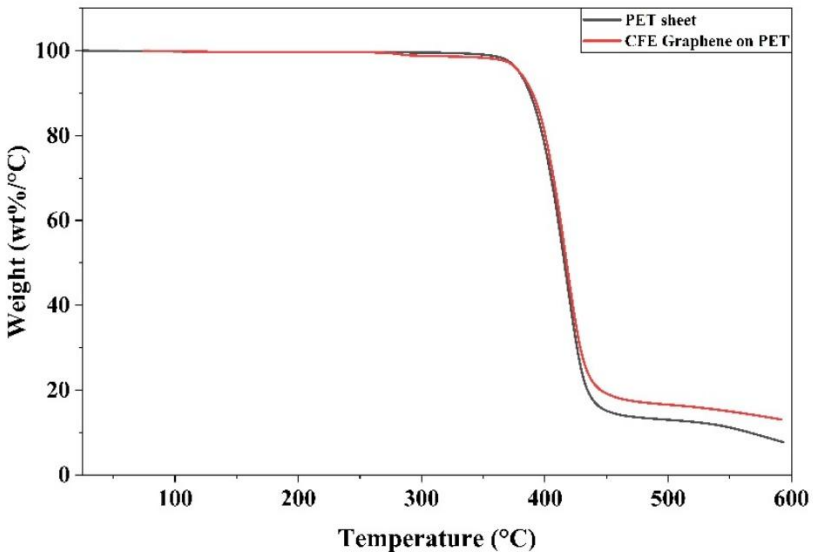

Figure 25: TGA analysis of CFE graphene coated on PET.

5.5 Comparison of Electrical performance with Literature

Polyimide (PI) is the most common substrate used for laser-induced graphene (LIG) due to its thermal stability and capability of forming graphene directly under laser exposure. However, the reported values of sheet resistance significantly depend on laser type and processing parameters. Bare PI processed using the CO_2 laser has been reported to yield sheet resistance within the range of 26–49 Ω/sq [91], whereas other works claimed values up to 100–250 Ω/sq [92]. Very low values of ~5 Ω/sq were obtained in the optimized cases [93], but the majority of results are still within the range of 10–100 Ω/sq. Higher-order sources, such as picosecond pulsed lasers sources, claimed values of 36.6 Ω/sq [94]. Modified PI films using other materials, such as copper-layered PI films, were found to yield 8.4–62 Ω/sq [95].

The formation of sp^2 carbon (graphene-like structures) versus amorphous carbon upon laser treatment of materials like polyimide (PI) largely depends on the chemical composition.

Materials rich in aromatic groups and carbonyl functionalities, such as PI, easily form sp^2 hybridized carbon during laser irradiation. The laser induces localized pyrolysis by breaking weaker bonds (e.g., C–O, C–H) and removing oxygen and hydrogen atoms through deoxygenation and dehydrogenation reactions. This process promotes the rearrangement of carbon atoms into stable, conjugated aromatic rings characteristic of graphene's hexagonal lattice. Aromatic rings and carbonyl groups provide pre-existing sp^2 structures and conjugated π-electrons that facilitate the formation of continuous sp^2 carbon networks during laser annealing. The π-bonding stabilizes planar hexagonal carbon rings, favouring crystalline graphitic domains over amorphous carbon [107].

In comparison, our CFE graphene-coated PET film achieved a sheet resistance of 16.17 Ω/sq at 10 µm thickness. This is significantly comparable to the majority of PI-based works. For example, when comparing with widely documented values of 26–49 Ω/sq [91] or 10–100 Ω/sq [96].

Table 8: Comparison of the sheet resistance achieved with CFE graphene with the literature.

Substrate	**Precursor Material**	**Film Thickness (µm)**	**Sheet Resistance (Ω/sq)**	**Laser Type**	**Reference**
PI	Bare PI	~15–60	26–49	CO_2 Laser	[91]
PI	Bare PI	Not reported	~5	CO_2 Laser	[92]
PI	Bare PI	Not reported	100–250	CO_2 Laser	[93]
PI (Kapton, DuPont)	Bare PI	~10	36.6	Picosecond Laser (1064 nm)	[94]
PI	Bare PI	Not reported	5–20	CO_2 Laser	[95]
PI	Bare PI	Not reported	5	CO_2 Laser	[96]
PI	Bare PI	>>125	Not reported	CO_2 Laser	[97]
PI	Bare PI	Not reported	10–100	CO_2 Laser	[98]
PI	Bare PI	Not reported	15	CO_2 Laser	[99]

PI (Kapton, DuPont)	Bare PI	Not reported	62	CO_2 Laser	[100]
PI (Kapton, DuPont)	Kapton PI	Not reported	Not reported	CO_2 Laser	[101]
Polylactic Acid (PLA)	Kapton PI	35–47	17.1–18.9	CO_2 Laser	[102]
PI with Cu layering	PI layer in FCCL	<10	8.4–62	CO_2 Laser	[103]
PET	**CFE Graphene coating**	**10**	**16.17**	**Blue Laser (450 nm)**	**This work**

The reason for this improved performance is that the CFE graphene coating provides an initial conductive framework on the PET substrate. When exposed to laser treatment, this coating undergoes further structural transformation, producing a highly interconnected network of graphene pathways. Taken together, these results clearly highlight that PET (Table 9), when combined with a CFE graphene coating and laser carbonization, can achieve comparable electrical performance compared to PI. Along with its other advantages such as lower cost, lightweight nature, recyclability, and suitability for large-scale processing, PET emerges as a strong candidate for use in flexible and transient electronic applications (Table 9). This includes devices such as single-use sensors, RFID tags, and other biodegradable or recyclable electronics, where both high conductivity and sustainability are essential.

Table 9: Comparison between PI and PET

Parameters	PI (Polyimide)	PET (Polyethylene Terephthalate)
Cost	High ($150–200/kg)	Low ($2–5/kg)
Recyclability	Difficult to recycle	Widely recyclable
Laser Compatibility	Forms LIG directly (no coating needed)	Needs graphene coating
Sheet Resistance Achievable	4–30 Ω/sq typical for PI-LIG	16.17 Ω/sq (in our case)
Scalability	Less scalable due to high material cost	Highly scalable – low cost and easy processing

In the above table the cost of the graphene coating applied to the PET sheet is not included in the comparative table because the exfoliation and preparation of the graphene were conducted using proprietary in-house CFE equipment. The detailed process parameters such as nozzle structure, flow rates, and pressure or temperature are protected by intellectual property and are not disclosed. However, for reference, the cost of the commercial graphene ink is approximately $69.00 for 25mL.

Chapter 6: RFID Antenna Fabrication and Testing

6.1 RFID Working Principle

An RFID tag, often referred to as a transponder, is a small gadget that may be connected to an object in order to monitor and identify it. Within a tag, the sub-systems consist of a substrate or encapsulating material, an antenna, and a microchip. Whereas the antenna transmits and receives data, the microchip stores data. RFID tags are classified as either active or passive depending on the power source. To power the integrated chip (IC), active tags need a battery, but passive tags use the voltage created by an electromagnetic field flux produced by the reader. A reader and a tag make up an RFID system. An interrogation signal is generated and transmitted to the tag by the reader. By using electromagnetic wave capture and magnetic induction (near-field coupling), the reader powers a passive tag (Figure 26).

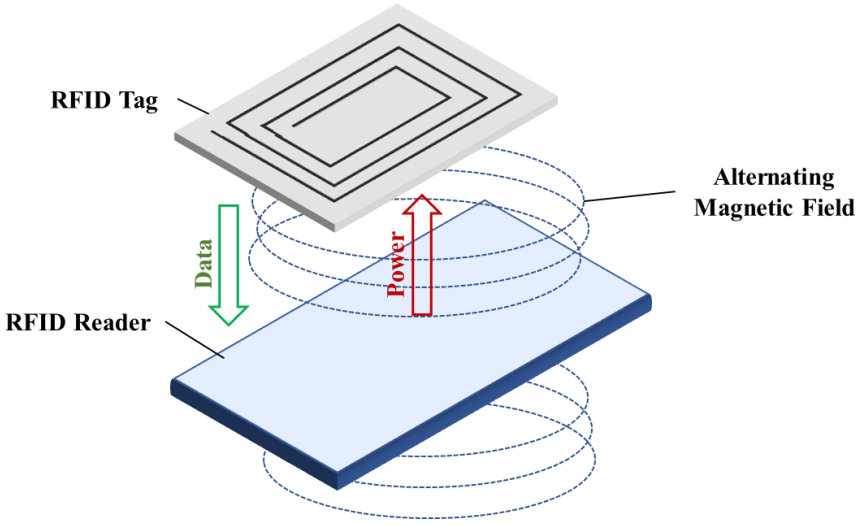

Figure 26: Schematics of RFID system consisting of an RFID tag and RFID reader.

Faraday's law states that a time-varying magnetic field over a surface that is bounded by a closed path creates a voltage around the loop. When the reader and tag are close to one another, the reader antenna coil's time-varying magnetic field (B) causes the closed tag antenna coin to create a voltage at the same frequency. Current flows through the coil as a result of the voltage that is created there. The induced voltage on the tag antenna coil is equal to the temporal rate of change (ψ) of the magnetic flux. The induced voltage is displayed in Equation 6.1, where N is the number of coil turns.

(Eq. 6.1) $$Vo = -N\frac{d\psi}{dt}$$

The following are the equations for the produced magnetic field (B) that results from current (I) flowing in the reader coil.

(Eq.6.2) $$I = Io\sin(wt)$$

(Eq.6.3) $$B = Bo\sin(wt)$$

Then, the voltage induced in tag coil is:

(Eq.6.4) $$V = Vo\sin(wt)$$

6.2 RFID Geometry Optimization Based on the Inductance and Resistance

A current carrying conductor's self-inductance is represented by the ratio of the magnetic flux it produces to the current flowing through it, as indicated by Equation 6.5. In this equation, i is the current (Amp) and Φ is the magnetic flux (Weber).

(Eq.6.5)
$$L = \frac{\Phi(i)}{i}$$

The inductance of a coil spiral has been estimated using a number of different formulae [71], [72]. In Figure 6.2, the L for a square coil is approximated using Equation 6.6, which is taken from [73].

(Eq.6.6)
$$L = \frac{1.27\mu n^2 davg}{2}\left[\ln\left(\frac{2.07}{\varphi}\right) + 0.18\varphi + 0.13\varphi^2\right]$$

In this equation, n represents the number of turns, while $d0$ and di represent the coil's outer and inner diameters, as seen in figure 6.2. $davg$ is the average of inner and outer diameters (($d0$ + di)/2) and φ is the fill factor, using the following formula.

(Eq.6.7)
$$\varphi = \frac{do - di}{do + di}$$

In order to determine the square coil RFID antenna's end-to-end resistance, the conductance trace's total length, lc, needs be determined as a function of coil geometry, which is as follows.

(Eq.6.8)
$$lc = 4ndo - 4nw - (2n+1)^2 (s + w)$$

By substituting the Equation 6.8 to Equation 4.2, the end-to-end resistance will be as follows.

(Eq.6.9)
$$R = Rs\frac{lc}{w}$$

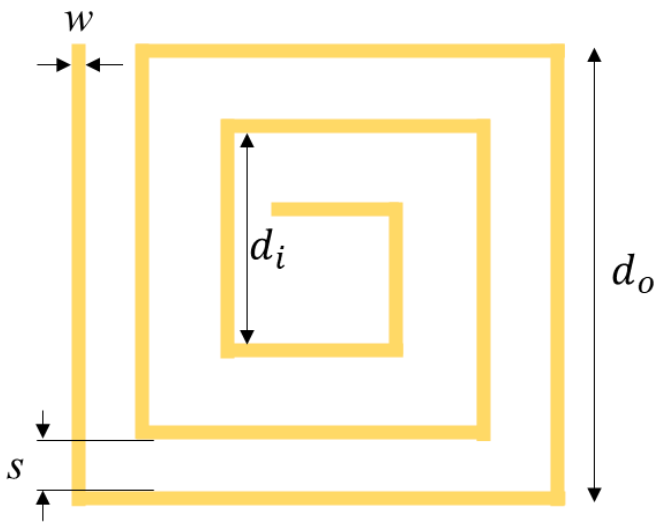

Figure 27: Coil Geometry for the RFID Tag

Equation 6.6 indicates that increasing the number of turns improves the coil's performance by increasing the inductance. nevertheless, it is clear from Equations 6.8 and 6.9 that as the number of turns grows, so does the coil's end-to-end resistance. The resistance should be kept as low as feasible in order to increase the current produced by the induced voltage in the coil. To determine the optimal number of turns in this context, a simple optimization method was applied. In this context, the inductance and conductance (1/R) as a function of coil turns can be calculated and shown using a MATLAB code (see to the Appendix section). The two curves intersect nearly at n = 6 as the optimum point, as illustrated in Figure 28.

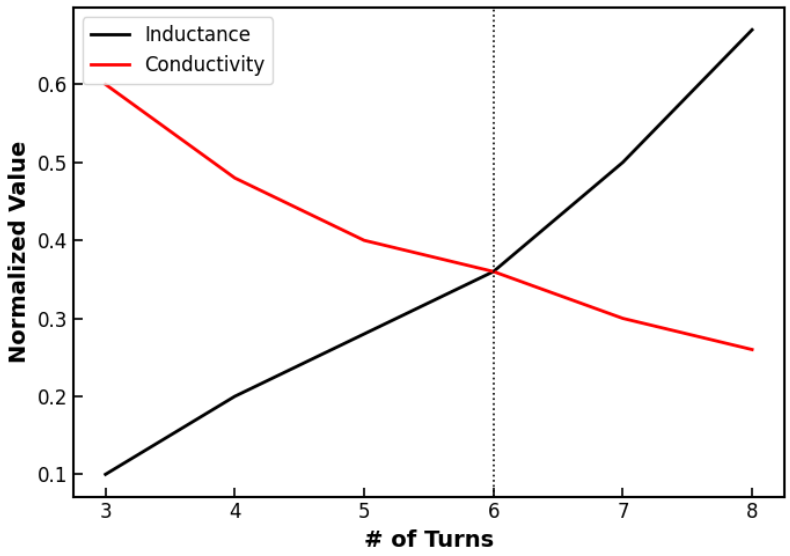

Figure 28: Optimization of number of coil's turns based on inductance and conductivity of the RFID.

6.3 RFID Proof-of-Concept

After optimizing electrical properties and shape, an RFID antenna tag was created. A material with low sheet resistance (CFE Graphene) was coated on a PET substrate. The laser-scribed square coil RFID was fabricated using the same laser settings (80% power and 500 mm/min speed). Figure 25 depicts a laser-patterned, coil-shaped RFID antenna. The tag is 50 × 50 mm and has six turns with one mm wide line (Figure 29).

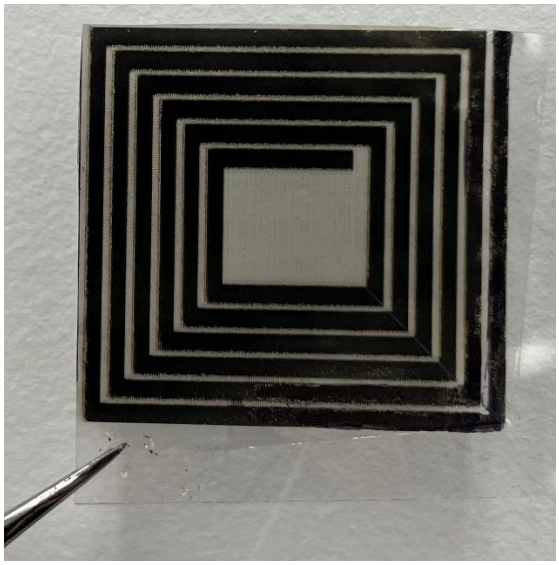

Figure 29: Optical image of the 6-turn laser-scribed RFID tag.

Figures 30 (b) demonstrate the RFID antenna's application. A reader (white object) creates a magnetic field that induces a current in the RFID antenna. To create a wireless data transfer connection with the reader in an actual RFID tag, an integrated chip (IC) is powered by the induced current.

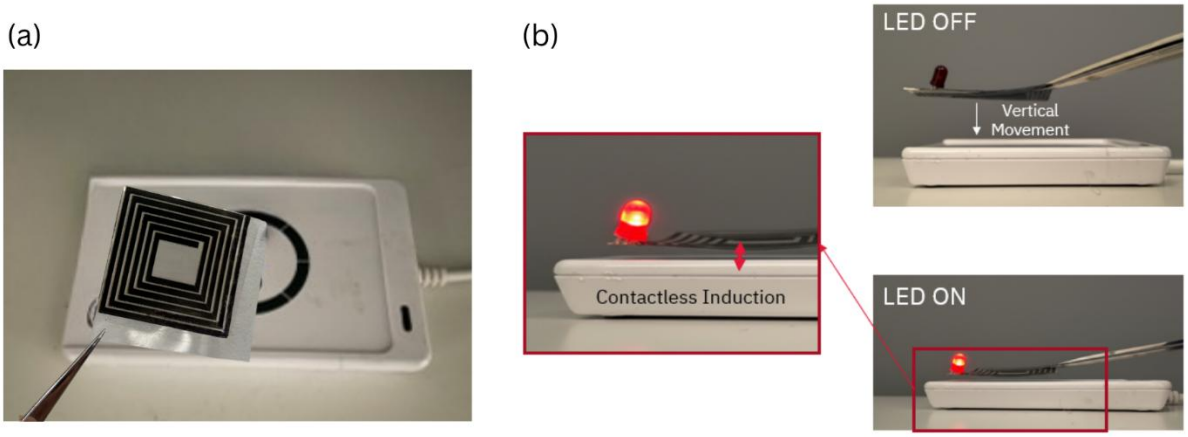

Figure 30: (a) Laser-scribed RFID tag and RFID Reader, (b) Optical image of the Vertical movement of the tag toward the surface of the RFID reader where the maximum electromagnetic flux occurs making the LED turns on.

To test the contactless induction and operation of the manufactured RFID antenna, an LED was mounted to the two ends and exposed to a commercial RFID reader (Figure 31). The LED was attached directly to the two ends of the laser-induced graphene (LIG) antenna coil. Each leg of the LED was positioned on the respective terminal of the coil, and a small amount of conductive glue was applied at the contact points. This conductive adhesive not only fixed the LED in place mechanically but also ensured good electrical connectivity between the antenna ends and the LED legs. After curing at room temperature, the glue formed stable junctions that allowed the induced current from the RFID reader to pass through the LED, causing it to light up when the antenna was brought into the reader's field. The LED switched on/off gradually as the antenna moved horizontally and vertically towards the center of the reader, where greatest electromagnetic flux occurs. Figure 30 (b) shows contactless induction, as evidenced by the LED remaining on despite a visible gap between antenna and reader.

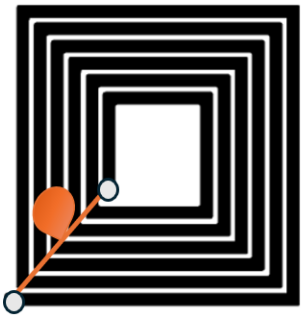

Figure 31: Schematic showing how LED is attached to the ends of the coil.

6.4 Transient Property

An RFID tag printed on PET was submerged in room temperature distilled water in turbulent settings (120 rpm) to illustrate the films' transitory and recyclable qualities (Figure 32). The carbonized areas of the film (coil-shaped RFID) adhere to the substrate, whereas the unexposed, non-carbonized portions of the film are readily dissolved in water due to the intrinsic hydrophilicity of the fundamental graphene components. However, because of a structural bond with the unexposed portions of the film, the carbonized portions are partially dragged into the aqueous phase upon transfer into the water. During immersion, the substrate gradually swells and weakens, making it possible to detach the circuit layer. After 15 minutes, the uncarbonized graphene coating begins to detach from the PET surface. After 30 minutes, the PET substrate was completely removed from the beaker, leaving behind only a small quantity of detached uncarbonized graphene, which is barely visible in the water due to its low concentration. The final image (top right) confirms the successful recovery of the PET film with the carbonized pattern intact. This process demonstrates that the uncarbonized precursor can be separated during immersion, while the laser-carbonized regions remain stable, underlining the recyclability and selective removal capability of the system.

Concerns about the biodegradability of graphene and its environmental impact once it dissolves or disperses into water are important considerations for sustainable applications. Research has shown that graphene-based materials, including graphene oxide, can be biodegraded by natural environmental processes involving specific bacteria, fungi, and insects. These organisms can

enzymatically break down graphene materials into smaller fragments or convert them into carbon dioxide and biomass, thus reducing their persistence and potential pollution in ecosystems [106].

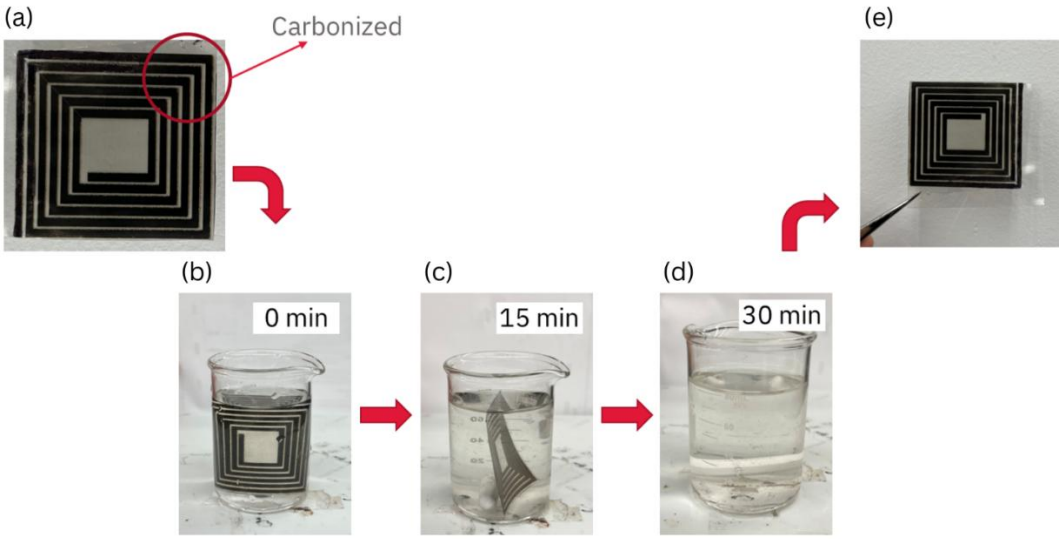

Figure 32: Dipping RFID antenna tag in DI water. (a) The carbonized coil-shaped RFID pattern printed on PET, where carbonized regions adhere strongly to the substrate, while uncarbonized precursor regions remain hydrophilic. (b) The device submerged in distilled water at 0 min under turbulent conditions (120 rpm), initiating substrate swelling and dissolution of uncarbonized areas. (c) After 15 min, partial detachment of the uncarbonized coating is observed as the PET substrate weakens and begins releasing non-carbonized graphene. (d) After 30 min, the PET film is removed from the beaker, leaving behind only traces of dispersed uncarbonized graphene in the aqueous medium. (e) recovered PET substrate with intact carbonized pattern, ready for recycling.

Chapter 7: Conclusion and Future Work

7.1 Summary of Technological and Environmental Findings

This thesis investigates sustainable material platforms for the development of transient and flexible electronics, with a particular focus on applications such as single-use RFID devices. The research is divided into two complementary studies.

The first study explores cellulose substrates coated with graphene oxide (GO) and lignin-based mixtures. Cellulose was chosen for its natural biodegradability and flexibility, while lignin served as a carbon-rich additive to improve the electrical performance of the coatings. By applying laser carbonization to these precursors, conductive patterns were generated directly on the cellulose surface. This approach demonstrates how biodegradable and compostable materials can be engineered to provide transient electronic components that degrade naturally after use, offering a clear pathway toward environmentally responsible electronics.

The second study focuses on polyethylene terephthalate (PET) substrates coated with compressible flow exfoliated (CFE) graphene. In this case, the PET film provided mechanical strength and flexibility, while the CFE graphene layer acted as an initial conductive framework. Subsequent laser carbonization further enhanced the conductivity, resulting in films with low sheet resistance values (~16.17 Ω/sq). This system highlights the potential of combining scalable graphene coating methods with laser processing to achieve high-performance flexible circuits.

Together, these two material strategies provide a balance between biodegradability/recyclability, manufacturing freedom, and high conductivity, forming the guiding objectives of this work. The

cellulose-based system addresses the demand for environmentally friendly, transient devices, while the PET/CFE graphene system offers superior electrical performance suitable for robust and flexible electronic applications. By uniting these approaches, the thesis contributes to the design of next-generation sustainable electronic devices that reduce environmental impact without compromising on functionality.

7.2 Challenges and Limitations

Despite these advancements, several challenges must be addressed to enable large-scale deployment of such technologies:

- The PET substrate, which currently is not biodegradable, can be replaced with a substrate with transient properties, and shows biodegradability. Alternatives such as cellulose, nanocellulose, lignin-based films, or silk fibroin are now being explored because they offer similar flexibility but can naturally degrade, making them more sustainable choices.
- Although we produced one of the greatest electrical conductivities in the literature, it is still significantly lower than metals. For example, aluminum has an electrical conductivity of 3.5×10^{7} S/m, whereas our work has 6.19×10^{3} S/m. Nanofillers, including carbon nanodots, might help achieve this approach.

- **Scalability** remains a major issue, as laser carbonization are currently limited to laboratory-scale setups. Future research must adapt these processes for **roll-to-roll manufacturing**.
- **Film uniformity and pattern resolution** vary depending on process parameters and require severe control mechanisms to ensure consistent performance.

- The **long-term operational stability** of biodegradable electronics, especially in varying humidity and temperature conditions, remains insufficiently studied and may impact distribution in outdoor or industrial settings.

7.4 Future Directions

To fully harness the potential of biodegradable RFID electronics, several research avenues can be explored:

- Better conductivity can be achieved by further optimizing laser power and speed combinations and refining precursor formulations..
- Development of **multi-layer circuit architectures** using stacked or patterned biodegradable films for more complex functionalities.
- Integration of **wireless sensing capabilities** such as temperature or humidity monitoring within transient tags for smart agricultural or logistics applications.
- Advancement of **biodegradability testing frameworks**, including accelerated aging studies and real-world deployment evaluations to better understand material behaviour across environmental scenarios.
- Exploration of **biodegradable semiconductors and batteries** to complement carbonized conductors and build fully transient electronic systems from end to end.

This chapter concludes the thesis by emphasizing the viability of graphene films in advancing sustainable electronics and by outlining practical steps to transition from laboratory innovation to industrial application.

Appendix - Optimization MATLAB Code

```
clc; clear;


% Parameters

muθ = 4e-7*pi;       % Air permeability (H/m)

fθ = 13.56e6;        % Target frequency (Hz)

Rs = 2.8;            % Sheet resistance (Ω/sq)

n  = 6;              % Number of turns

do = 50;             % Outer dimension (mm)

w  = 2.0;            % Trace width (mm)

s  = 1.0;            % Spacing (mm)

% Geometry

di  = do - 2*w*n - s*(2*n-2);

dav = (do + di)/2;

phi = (do - di)/(do + di);

dav_m = dav*1e-3;

% Inductance

L = muθ * n^2 * dav_m * (log(2.07/phi) + 0.18*phi + 0.13*phi^2);

L_uH = L*1e6;

% Resistance

lc = 4*n*do - (2*n+1)^2*(s+w);

R  = Rs * (lc / w);

% Tuning capacitor

C = 1 / ((2*pi*fθ)^2 * L);

C_pF = C*1e12;

% Results

fprintf('Inductance = %.2f μH\n', L_uH);

fprintf('Resistance = %.2f Ω\n', R);
```

fprintf('Capacitance = %.2f pF\n', C_pF);

\end{lstlisting}

REFERENCES

1. A. Ashiq, P. Huang, J. Young, A. Gallego-Schmid, R. Price, and M. P. Shaver, "Technical and environmental assessment of end-of-life scenarios for plastic packaging with electronic tags," Resources, Conservation and Recycling, vol. 201, p. 107341, Feb. 2024.
2. C. P. Balde, V. Forti, V. Gray, R. Kuehr, and P. Stegmann, The Global E-waste Monitor 2017: Quantities, Flows and Resources. United Nations University, 2017.
3. L. Chen, X. Wang, J. Li, and M. Zhang, "The environmental benefits and burdens of RFID systems in Li-ion battery supply chains – An ex-ante LCA approach," Journal of Cleaner Production, vol. 422, p. 139351, 2024.
4. United Nations Environment Programme, "The Circular Economy and Electronic Waste: Global Strategies and Best Practices 2023," UNEP, Nairobi, Kenya, 2023.
5. P. Agreement, "Paris agreement," in Rep. Conf. Parties United Nations Framework Convention on Climate Change (COP21, Paris), vol. 4, p. 2017.
6. M. N. Hamidon, T. D. Farnana, I. H. Hasan, A. Sali, and M. Md. Isa, “Printing of passive RFID tag antennas on flexible substrates for long read distance applications: Materials and techniques,” Journal of Science: Advanced Materials and Devices, vol. 9, no. 4, p. 100778, Dec. 2024.
7. D. Akinwande, N. Petrone, and J. Hone, "Two-dimensional flexible nanoelectronics," Nat. Commun., vol. 5, p. 5678, 2014.
8. M. Wang, Z. Li, and H. Chen, "Roll-to-roll gravure printed large-area flexible carbon nanotube synaptic photogating transistor arrays," Carbon, vol. 201, pp. 123-134, 2023.
9. R. Li, L. Wang, and L. Yin, “Materials and Devices for Biodegradable and Soft Biomedical Electronics,” Materials, vol. 11, no. 11, Art. no. 2108, Oct. 2018

10. M. F. Ashby and K. Johnson, Materials and Design: The Art and Science of Material Selection in Product Design, 3rd ed. Butterworth-Heinemann, 2013.
11. A. R. Bhattacharyya, S. K. Saha, and S. Banerjee, "Effect of laser wavelength on reduction of graphene oxide films," Appl. Surf. Sci., vol. 598, p. 153780, 2022.
12. E. Lizundia et al., "Multifunctional lignin-based nanocomposites and nanohybrids," Green Chemistry, vol. 23, no. 21, pp. 8629-8656, 2021.
13. F. Bonaccorso, Z. Sun, T. Hasan, and A. C. Ferrari, "Graphene photonics and optoelectronics," Nat. Photon., vol. 4, pp. 611–622, 2010.
14. Q. Luo, T. Zeng, K. Gu, Q. Lin, and W. Yang, "Research Progress of Lignin-Derived Functional Materials for Electrochemical Energy Storage," ACS Applied Energy Materials, vol. 7, no. 24, pp. 11610-11632, Oct. 2024.
15. A. Costanzo, V. Passaro, and F. Minucci, "Is laser-induced graphene (LIG) environmentally sustainable? Laboratory-scale life cycle assessment of LIG from petroleum- and bio-derived precursors," Journal of Cleaner Production, vol. 453, p. 140352, 2025.
16. X. Cao, Y. Shi, and W. Hong, "Recent progress in two-dimensional materials for flexible and wearable electronics," Adv. Funct. Mater., vol. 31, no. 39, p. 2102102, 2021.
17. H. Saleem, M. Haneef, and H. Y. Abbasi, "Synthesis route of reduced graphene oxide via thermal reduction of chemically exfoliated graphene oxide," Mater. Chem. Phys., vol. 204, pp. 1–7, 2018.
18. H.-H. Huang, K. K. H. De Silva, G. R. A. Kumara, and M. Yoshimura, "Structural evolution of hydrothermally derived reduced graphene oxide," Sci. Rep., vol. 8, no. 1, pp. 1–9, 2018
19. M. G. Franklin, H. Al-Banna, K. V. Nguyen, M. J. Khan, and A. R. Crook, "Cellulose-Based Laser-Induced Graphene Devices for Electrochemical Monitoring of Bacterial Phenazine

Production and Viability," ACS Applied Materials & Interfaces, vol. 15, no. 10, pp. 12536–12545, 2023.

20. Z. Chen, W. Ren, and H.-M. Cheng, "Graphene-based materials for bioelectronics," Adv. Mater., vol. 27, no. 5, pp. 783–798, 2015.
21. R. Y. N. Gengler et al., “Revealing the ultrafast process behind the photoreduction of graphene oxide,” Nat. Commun., vol. 4, no. 1, pp. 1–5, 2013.
22. Y. C. Guan, Y. W. Fang, G. C. Lim, H. Y. Zheng, and M. H. Hong, “Fabrication of laser-reduced graphene oxide in liquid nitrogen environment,” Sci. Rep., vol. 6, no. 1, pp. 1–7, 2016
23. N. B. Erdal and M. Hakkarainen, “Degradation of Cellulose Derivatives in Laboratory, Man-Made, and Natural Environments,” Biomacromolecules, vol. 23, no. 7, pp. 2713-2729, Jun. 2022.
24. C. Dagdeviren, S. W. Hwang, Y. Su, S. Kim, H. Cheng, O. Gur, R. Haney, F. G. Omenetto, Y. Huang, and J. A. Rogers, “Transient, biocompatible electronics and energy harvesters based on ZnO,” Small, vol. 9, no. 20, pp. 3398-3404, Oct. 2013.
25. L. Dai, D. W. Chang, and J.-B. Baek, "Carbon nanomaterials for advanced energy conversion and storage," Small, vol. 8, no. 8, pp. 1130–1166, 2012.
26. A. Di Bartolomeo, F. Giubileo, F. Romeo, P. Sabatino, G. Carapella, L. Iemmo, T. Schroeder, and G. Lupina, “Graphene field effect transistors with Niobium contacts and asymmetric transfer characteristics,” Nanotechnology, vol. 26, no. 47, Art. no. 475202, Nov. 2015.
27. N. Wei, W. Xu, S. Li, and J. Shi, “Sustainable depolymerization of lignin into aromatic compounds using amphiphilic Anderson-type polyoxometalate catalysts,” Int. J. Biol. Macromol., vol. 277, pt. 2, Art. no. 133257, Oct. 2024.

28. Y. Du, J. Chen, and J. Li, "Laser-induced graphene: Preparation, properties, and applications," Sci. Bull., vol. 61, no. 19, pp. 1513–1533, 2016.

29. A. C. Ferrari and D. M. Basko, "Raman spectroscopy as a versatile tool for studying the properties of graphene," Nat. Nanotechnol., vol. 8, pp. 235–246, 2013.

30. A. C. Ferrari and J. Robertson, "Interpretation of Raman spectra of disordered and amorphous carbon," Phys. Rev. B, vol. 61, no. 20, pp. 14095–14107, 2000.

31. E. Fortunato, P. Barquinha, and R. Martins, “Oxide semiconductor thin-film transistors: A review of recent advances,” Adv. Mater., vol. 24, no. 22, pp. 2945–2986, May 2012.

32. R. S. N. Kumar, A. V. Ramirez, P. Verding, P. Nivelle, F. Renner, J. D’Haen, and W. Deferme, “Deposition of ultra-thin coatings by a nature-inspired Spray-on-Screen technology,” Commun. Eng., vol. 2, Art. no. 42, Jun. 2023.

33. J. Xu, D. K. Dang, V. T. Tran, X. Liu, J. S. Chung, S. H. Hur, W. M. Choi, E. J. Kim, and P. A. Kohl, “Liquid-phase exfoliation of graphene in organic solvents with addition of naphthalene,” J. Colloid Interface Sci., vol. 418, pp. 37–42, Mar. 2014.

34. A. K. Geim, "Graphene: Status and prospects," *Science*, vol. 324, no. 5934, pp. 1530–1534, 2009.

35. A. K. Geim and K. S. Novoselov, "The rise of graphene," *Nat. Mater.*, vol. 6, pp. 183–191, 2007.

36. M. R. Lukatskaya, O. Mashtalir, C. E. Ren, Y. Dall’Agnese, P. Rozier, P. L. Taberna, M. Naguib, P. Simon, M. W. Barsoum, and Y. Gogotsi, “Conductive two-dimensional titanium carbide ‘clay’ with high volumetric capacitance,” Science, vol. 341, no. 6153, pp. 1502–1505, Sep. 2013.

37. M. F. El-Kady and R. B. Kaner, “Scalable fabrication of high-power graphene micro-supercapacitors for flexible and on-chip energy storage,” Nat. Commun., vol. 4, no. 1, pp. 1–9, 2013.

38. J. D. Majumdar and I. Manna, Laser-assisted fabrication of materials, vol. 161. Springer Science & Business Media, 2012.

39. J. Lin et al., “Laser-induced porous graphene films from commercial polymers,” Nat. Commun., vol. 5, no. 1, pp. 1–8, 2014.

40. H. Liu et al., “Laser-oxidized Fe3O4 nanoparticles anchored on 3D macroporous graphene flexible electrodes for ultrahigh-energy in-plane hybrid microsupercapacitors,” Nano Energy, vol. 77, p. 105058, 2020.

41. B. Kulyk et al., “Laser-induced graphene from paper for mechanical sensing,” ACS Appl. Mater. Interfaces, vol. 13, no. 8, pp. 10210–10221, 2021. 62

42. M. Yuan et al., “Facile and scalable fabrication of high-performance microsupercapacitors based on laser-scribed in situ heteroatom-doped porous graphene,” ACS Appl. Mater. Interfaces, vol. 13, no. 19, pp. 22426–22437, 2021.

43. M. Yuan et al., “Laser synthesis of superhydrophilic O/S co-doped porous graphene derived from sodium lignosulfonate for enhanced microsupercapacitors,” J. Power Sources, vol. 513, p. 230558, 2021.

44. Y. Lei, A. H. Alshareef, W. Zhao, and S. Inal, “Laser-Scribed Graphene Electrodes Derived from Lignin for Biochemical Sensing,” ACS Appl. Nano Mater., vol. 3, no. 2, pp. 1166–1174, Feb. 2020, doi: 10.1021/acsanm.9b01795.

45. S. Evlashin et al., “Controllable Laser Reduction of Graphene Oxide Films for Photoelectronic Applications,” ACS Appl. Mater. Interfaces, vol. 8, no. 42, pp. 28880–28887, Oct. 2016, doi: 10.1021/acsami.6b10145.
46. T. X. Tran et al., “Laser-induced reduction of graphene oxide by intensitymodulated line beam for supercapacitor applications,” ACS Appl. Mater. Interfaces, vol. 10, no. 46, pp. 39777–39784, 2018.
47. J.-X. Yan et al., “Highly Conductive Graphene Paper with Vertically Aligned Reduced Graphene Oxide Sheets Fabricated by Improved Electrospray Deposition Technique,” ACS Appl. Mater. Interfaces, vol. 11, no. 11, pp. 10810– 10817, Mar. 2019, doi: 10.1021/acsami.8b19811.
48. B. Jiang et al., “Lignin as a wood-inspired binder enabled strong, water stable, and biodegradable paper for plastic replacement,” Adv. Funct. Mater., vol. 30, no. 4, p. 1906307, 2020.
49. Y. Chyan, R. Ye, Y. Li, S. P. Singh, C. J. Arnusch, and J. M. Tour, “Laserinduced graphene by multiple lasing: toward electronics on cloth, paper, and food,” ACS Nano, vol. 12, no. 3, pp. 2176–2183, 2018.
50. S. Park et al., “Fabrication of fanlike L-shaped graphene nanostructures with enhanced thermal/electrochemical properties via laser irradiation,” Carbon N. Y., vol. 182, pp. 691–699, 2021.
51. M. J. McAllister et al., “Single sheet functionalized graphene by oxidation and thermal expansion of graphite,” Chem. Mater., vol. 19, no. 18, pp. 4396–4404, 2007.

52. M. Yan, W. Huang, and Z. Li, “Chitosan cross-linked graphene oxide/lignosulfonate composite aerogel for enhanced adsorption of methylene blue in water,” Int. J. Biol. Macromol., vol. 136, pp. 927–935, 2019.
53. L. M. Malard, M. A. Pimenta, G. Dresselhaus, and M. S. Dresselhaus, “Raman spectroscopy in graphene,” Phys. Rep., vol. 473, no. 5–6, pp. 51–87, 2009.
54. M. Hepp et al., “Trained laser-patterned carbon as high-performance mechanical sensors,” npj Flex. Electron., vol. 6, no. 1, p. 3, Dec. 2022, doi: 10.1038/s41528- 022-00136-0. 63
55. F. M. Smits, “Measurement of sheet resistivities with the four-point probe,” Bell Syst. Tech. J., vol. 37, no. 3, pp. 711–718, 1958.
56. J. Y. Hwang et al., “Direct preparation and processing of graphene/RuO2 nanocomposite electrodes for high-performance capacitive energy storage,” Nano Energy, vol. 18, pp. 57–70, 2015.
57. J. Cai, A. Watanabe, and C. Lv, “Laser direct writing of carbon/Au composite electrodes for high-performance micro-supercapacitors,” in Laser-based Microand Nanoprocessing XI, 2017, vol. 10092, pp. 123–130.
58. V. B. Nam, J. Shin, A. Choi, H. Choi, S. H. Ko, and D. Lee, “High-temperature, thin, flexible and transparent Ni-based heaters patterned by laser-induced reductive sintering on colorless polyimide,” J. Mater. Chem. C, vol. 9, no. 17, pp. 5652–5661, 2021.
59. H. Wang et al., “Laser-carbonization: Peering into the formation of microthermally produced (N-doped) carbons,” Carbon N. Y., vol. 176, pp. 500–510, 2021.
60. Y. Li et al., “Laser-induced graphene in controlled atmospheres: from superhydrophilic to superhydrophobic surfaces,” Adv. Mater., vol. 29, no. 27, p. 1700496, 2017.

61. A. Balakrishnan, W. D. Palmer, W. T. Joines, and T. G. Wilson, “The inductance of planar structures,” in Proceedings Eighth Annual Applied Power Electronics Conference and Exposition, 1993, pp. 912–921.
62. H. M. Greenhouse, “Design of planar rectangular microelectronic inductors,” IEEE Trans. parts, hybrids, Packag., vol. 10, no. 2, pp. 101–109, 1974.
63. S. S. Mohan, M. del Mar Hershenson, S. P. Boyd, and T. H. Lee, “Simple accurate expressions for planar spiral inductances,” IEEE J. Solid-State Circuits, vol. 34, no. 10, pp. 1419–1424, 1999.
64. L. Teng, S. Ye, S. Handschuh-Wang, X. Zhou, T. Gan, and X. Zhou, “Liquid metal-based transient circuits for flexible and recyclable electronics,” Adv. Funct. Mater., vol. 29, no. 11, p. 1808739, 2019
65. X. Li, W. Cai, and R. S. Ruoff, "Large-area synthesis of high-quality and uniform graphene films on copper foils," *Science*, vol. 324, no. 5932, pp. 1312–1314, 2009.
66. F. Fantinelli Franco, M. H. Malik, L. Manjakkal, A. Roshanghias, C. J. Smith, and C. Gauchotte-Lindsay, “Optimizing carbon structures in laser-induced graphene electrodes using design of experiments for enhanced electrochemical sensing characteristics,” ACS Applied Materials & Interfaces, vol. 16, no. 47, pp. 65489–65502, Nov. 2024
67. K. Anagnostou, M. Urban, E. Sotiropoulos, et al., “Water-based graphene oxide inks for inkjet-printed flexible moisture energy generators,” Scientific Reports, vol. 15, art. no. 24685, 2025.
68. G. Lin, T. Zhou, Z. Zhou, and W. Sun, “Laser induced graphene for EMI shielding and ballistic impact damage detection in basalt fiber reinforced composites,” Composites Science and Technology, vol. 242, art. no. 110182, 2023

69. E. Svinterikos, I. Zuburtikudis, and M. Al-Marzouqi, “Electrospun lignin-derived carbon micro- and nanofibers: A review on precursors, properties, and applications,” ACS Sustainable Chemistry & Engineering, vol. 8, no. 37, pp. 13868–13893, Sept. 2020
70. M. Muddasar, M. Culebras, and M. N. Collins, “Lignin and its carbon derivatives: Synthesis techniques and their energy storage applications,” Materials Today Sustainability, vol. 28, p. 100990, 2024.
71. M. Lotya, Y. Hernandez, and J. N. Coleman, "Liquid phase production of graphene by exfoliation of graphite in surfactant/water solutions," *J. Am. Chem. Soc.*, vol. 131, no. 10, pp. 3611–3620, 2009.
72. S. Bai, L. Ruan, H. Chen, Y. Du, H. Deng, N. Dai, and Y. Tang, "Laser-induced graphene: Carbon precursors, fabrication mechanisms, material characteristics, and applications in energy storage," Chemical Engineering Journal, vol. 493, p. 144291, 2024.
73. D. C. Marcano, D. V. Kosynkin, and J. M. Tour, "Improved synthesis of graphene oxide," *ACS Nano*, vol. 4, no. 8, pp. 4806–4814, 2010.
74. Y. I. Zhang, L. Zhang, and C. Zhou, “Review of chemical vapor deposition of graphene and related applications,” Acc. Chem. Res., vol. 46, no. 10, pp. 2329– 2339, 2013.
75. H. Saleem, M. Haneef, and H. Y. Abbasi, “Synthesis route of reduced graphene oxide via thermal reduction of chemically exfoliated graphene oxide,” Mater. Chem. Phys., vol. 204, pp. 1–7, 2018.
76. H.-H. Huang, K. K. H. De Silva, G. R. A. Kumara, and M. Yoshimura, “Structural evolution of hydrothermally derived reduced graphene oxide,” Sci. Rep., vol. 8, no. 1, pp. 1–9, 2018.
77. R. Y. N. Gengler et al., “Revealing the ultrafast process behind the photoreduction of graphene oxide,” Nat. Commun., vol. 4, no. 1, pp. 1–5, 2013.

78. S. Pei, J. Zhao, J. Du, W. Ren, and H.-M. Cheng, “Direct reduction of graphene oxide films into highly conductive and flexible graphene films by hydrohalic acids,” Carbon N. Y., vol. 48, no. 15, pp. 4466–4474, 2010, doi: https://doi.org/10.1016/j.carbon.2010.08.006.
79. K. S. Novoselov, A. K. Geim, and I. V. Grigorieva, "Electric field effect in atomically thin carbon films," *Science*, vol. 306, no. 5696, pp. 666–669, 2004.
80. Z. Peng, J. Lin, R. Ye, E. L. G. Samuel, and J. M. Tour, “Flexible and stackable laser-induced graphene supercapacitors,” ACS Appl. Mater. Interfaces, vol. 7, no. 5, pp. 3414–3419, 2015.
81. S. Park and R. S. Ruoff, "Chemical methods for the production of graphenes," *Nat. Nanotechnol.*, vol. 4, pp. 217–224, 2009.
82. K. R. Paton, E. Varrla, and J. N. Coleman, "Scalable production of large quantities of defect-free few-layer graphene by shear exfoliation," *Nat. Mater.*, vol. 13, pp. 624–630, 2014.
83. Q. Hong, L. Yang, L. Ge, Z. Liu, and F. Li, “Direct-laser-writing of three-dimensional porous graphene frameworks on indium-tin oxide for sensitive electrochemical biosensing,” Analyst, vol. 143, no. 14, pp. 3327–3334, 2018.
84. S. Luo, P. T. Hoang, and T. Liu, “Direct laser writing for creating porous graphitic structures and their use for flexible and highly sensitive sensor and sensor arrays,” Carbon N. Y., vol. 96, pp. 522–531, 2016.
85. Q. Tian, W. Yan, Y. Li, and D. Ho, “Bean pod-inspired ultrasensitive and self-healing pressure sensor based on laser-induced graphene and polystyrene microsphere sandwiched structure,” ACS Appl. Mater. Interfaces, vol. 12, no. 8, pp. 9710–9717, 2020.
86. F. Qin and C. Brosseau, "A review and analysis of microwave absorption in polymer composites filled with carbonaceous particles," *J. Appl. Phys.*, vol. 111, no. 6, p. 061301, 2012.

87. M. M. Islam et al., "Self-Assembled Multifunctional Hybrids: Toward Developing High-Performance Graphene-Based Architectures for Energy Storage Devices," ACS Cent. Sci., vol. 1, no. 4, pp. 206-216, Jul. 2015.

88. C. N. R. Rao, A. K. Sood, and K. S. Subrahmanyam, "Graphene: The new two-dimensional nanomaterial," *Angew. Chem. Int. Ed.*, vol. 48, no. 42, pp. 7752–7777, 2009.

89. J.-X. Yan et al., "Highly Conductive Graphene Paper with Vertically Aligned Reduced Graphene Oxide Sheets Fabricated by Improved Electrospray Deposition Technique," ACS Appl. Mater. Interfaces, vol. 11, no. 11, pp. 10810– 10817, Mar. 2019.

90. J. A. Rogers, T. Someya, and Y. Huang, "Materials and mechanics for stretchable electronics," *Science*, vol. 327, no. 5973, pp. 1603–1607, 2010.

91. K. G. Mikheev, R. G. Zonov, and G. M. Mikheev, "The electrical resistance of laser-induced graphene synthesized by a continuous-wave CO_2-laser," *Phys. Solid State*, vol. 66, no. 6, pp. 875–881, Jun. 2024.

92. M. Abdulhafez, G. N. Tomaraei, and M. Bedewy, "Fluence-dependent morphological transitions in laser-induced graphene electrodes on polyimide substrates for flexible devices," *ACS Appl. Nano Mater.*, vol. 4, no. 3, pp. 2973–2986, Mar. 2021.

93. A. Sartanavičius, J. Žemgulytė, P. Ragulis, K. Ratautas, and R. Trusovas, "Laser-induced graphene in polyimide for antenna applications," *Crystals*, vol. 13, no. 7, p. 1003, Jun. 2023.

94. N. Dixit and S. P. Singh, "Laser-induced graphene (LIG) as a smart and sustainable material to restrain pandemics and endemics: A perspective," *ACS Omega*, vol. 7, no. 6, pp. 5112–5130, Feb. 2022.

95. V. Fiodorov, R. Trusovas, Z. Mockus, K. Ratautas, and G. Račiukaitis, “Laser-induced graphene formation on polyimide using UV to mid-infrared laser radiation,” *Polymers*, vol. 15, no. 21, p. 4229, Oct. 2023.

96. M. Liu, J. Wu, and H. Cheng, “Effects of laser processing parameters on properties of laser-induced graphene by irradiating CO_2 laser on polyimide,” *Sci. China Technol. Sci.*, vol. 65, no. 1, pp. 41–52, Jan. 2022.

97. J. de la Roche, I. López-Cifuentes, and A. Jaramillo-Botero, “Influence of lasing parameters on the morphology and electrical resistance of polyimide-based laser-induced graphene (LIG),” *Carbon Lett.*, vol. 33, pp. 587–595, Dec. 2023.

98. H. Liu, K. Chen, R. Wu, S. Pan, and C. Zhang, “Laser-induced graphene-based flexible substrate with photothermal conversion and photoresponse performance on polyimide film,” *ACS Appl. Mater. Interfaces*, vol. 15, no. 39, pp. 46550–46558, Sep. 2023.

99. A. Mostaccio, G. Antonelli, C. Occhiuzzi, E. Martinelli, and G. Marrocco, “Experimental characterization of laser induced graphene (LIG) antennas for S-band wearable applications in 5G,” in *Proc. IEEE Int. Conf. RFID Technology and Applications (RFID-TA)*, Cagliari, Italy, Sep. 2022.

100. I. R. Hristovski *et al.*, “Laser-induced graphene synthesis from the ultraviolet irradiation of polyimide using varied optical fluence,” in *Proc. SPIE 2D Photonic Materials and Devices VII*, vol. 12888, p. 1288804, Mar. 2024.

101. A. Velasco et al., "Laser-Induced Graphene Microsupercapacitors: Structure, Quality, and Electrochemical Performance," ACS Applied Materials & Interfaces, vol. 15, no. 8, pp. 12345–12356, 2023.

102. A. K. Singh, S. Shiby, A. Sahu, P. Pachori, M. Tanwar, R. Kumar, and I. A. Palani, “Parametric investigation on laser interaction with polyimide for graphene synthesis towards flexible devices,” J. Phys. D: Appl. Phys., vol. 56, no. 1, p. 015305, Jan. 2023.

103. J. Meng, W. Nie, K. Zhang, F. Xu, X. Ding, S. Wang, and Y. Qiu, “Enhancing electrochemical performance of graphene fiber-based supercapacitors by plasma treatment,” ACS Appl. Mater. Interfaces, vol. 10, no. 16, pp. 13652–13659, Apr. 2018.

104. M. Nazeri, Laser-induced graphene electrodes for organic electrochemical transistors (OECTs), M.A.Sc. thesis, Dept. Electr. Eng. Comput. Sci., York Univ., Toronto, ON, Canada, Dec. 2022.

105. R. Gholami, I. Lawan, P. Luengrojanakul, S. Ebrahimi, C.-H. Ahn, and S. Rimdusit, “Development of a laser induced graphene (LIG) and polylactic acid (PLA) shape memory polymer composite with simultaneous multi-stimuli response and deformation self-sensing characteristics,” *Nanoscale Adv.*, vol. 6, no. 17, pp. 4865–4876, Sep. 2024.

106. Z. Liu, J. Zhao, K. Lu, Z. Wang, L. Yin, H. Zheng, X. Wang, L. Mao, and B. Xing, "Biodegradation of Graphene Oxide by Insects (Tenebrio molitor Larvae): Role of the Gut Microbiome and Enzymes," *Environmental Science & Technology*, vol. 56, no. 23, pp. 16737–16747, 2022.

107. J. Lin, Z. Peng, Y. Liu, F. Ruiz-Zepeda, R. Ye, E. L. G. Samuel, M. J. Yacaman, B. I. Yakobson, and J. M. Tour, "Laser-induced porous graphene films from commercial polymers," Nature Communications, vol. 5, no. 5714, 2014.

108. Calculate Sheet Resistance Using the Four-Probe Method," Ossila, 2014. [Online]